

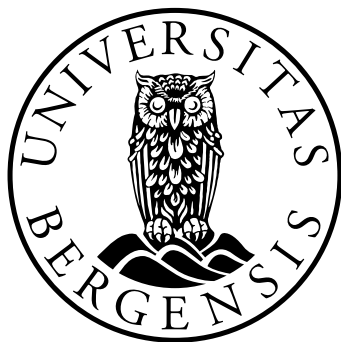
A Master's Thesis in Physical Oceanography

# Dispersion of Mine Particles in Førdefjorden

Sofie Arstein

October 2023

Geophysical Institute,  
University of Bergen



Institute of Marine Research





# Acknowledgements

A huge thanks to my supervisors, Mari and Lars, for the great guidance, and for all the encouraging and enthusiastic meetings and discussions. I am very grateful that my search for a master's project led me to you and IMR. Thank you for the opportunity to join a cruise and workshops. I have learned very much from working with you and this project, and I have truly enjoyed it!

I would like to thank Jon for running the Førdefjord160 model, Pål for making the LADIM setup and helping me with handling data, and Bjørn for always helping me with my Python problems. Thank you to everyone else at the Oceanography and Climate group at IMR for being welcoming and helpful.

Thanks to my fellow students at GFI for making these years of studying a blast! I very much appreciate all the coffee breaks, laughs, and great morning sessions at the bouldering gym. A special thanks to the balcony gang for the encouraging pep talks, and for helping me with whatever I needed.

Finally, thanks to my family and friends for the cheering and support throughout my studies. Thank you Erik for always being there for me, especially during the (lumpy) period of my masters.

Sofie Arstein  
Bergen, 10 October 2023



# Abstract

Førdefjorden is the site of a newly permitted submarine tailing disposal (STD) in Norway, and it is nationally debated. Major implications of an STD can be toxic compounds of the tailing, severe impacts on the benthic infauna, and dispersion of the tailing in the water masses. The most fine-grained particles have low sinking velocity and can potentially disperse far away from the STD site. It is crucial to understand the dynamics at the STD site to determine the spread of the tailing. In this thesis, I study the dispersion of fine-grained particles in Førdefjorden using data from the hydrodynamic fjord model Førdefjord160, which applies ROMS, and the particle tracking model LADIM. I evaluate the hydrodynamic model's performance compared to observations, and investigate the effect of changing the bathymetry and the release depths on the particle dispersion through four scenarios. The two first scenarios represent the early stages of the permitted STD with today's bathymetry and release depths close to the basin bottom. The third scenario represents the end of the STD, while the last scenario is an extreme case. The latter two scenarios have release depths higher up in the water column and a shallower bottom at the STD site. The validation implies that the model does not entirely capture the higher current speed values, nonetheless, it presents a realistic current field in the fjord. I find that particles drift further with decreasing release depths and a shallower bathymetry. I consider the fine fraction in regard to the regulations of the permitted STD and find that there is a pronounced amount of annual sedimentation in all scenarios. Daily concentrations of particles in the water masses are frequently close to or exceeding the set limits. The fine fraction of the annual tailing discharge can lead to high values of sedimentation and concentration, and it should be investigated further prior to the start of the STD in Førdefjorden.



# Contents

|  |            |
|--|------------|
| <b>Acknowledgements</b>  | <b>iii</b> |
| <b>Abstract</b>  | <b>v</b>   |
| <b>1 Introduction</b>  | <b>1</b>   |
| <b>2 Background</b>  | <b>5</b>   |
| 2.1 Coast-fjord water exchange . . . . .                                   | 5          |
| 2.2 Rotational dynamics . . . . .  | 7          |
| <b>3 Material and methods</b>  | <b>9</b>   |
| 3.1 Study Area . . . . .   | 9          |
| 3.2 Hydrodynamic fjord model . . . . .                                     | 10         |
| 3.3 Particle tracking model . . . . .                                      | 11         |
| 3.3.1 Setup for the scenarios . . . . .                                    | 12         |
| 3.4 Measurements . . . . .   | 12         |
| 3.4.1 Current measurements . . . . .                                       | 12         |
| 3.4.2 Hydrographic measurements . . . . .                                  | 13         |
| 3.5 Wind data . . . . .  | 13         |
| 3.6 Sedimentation and concentration calculations . . . . .                 | 14         |
| <b>4 Results</b>   | <b>17</b>  |
| 4.1 Validation of Førdefjord160 . . . . .                                  | 17         |
| 4.1.1 Hydrography . . . . .  | 17         |
| 4.1.2 Selecting grid points for current field validation . . . . .         | 20         |
| 4.1.3 Current field validation . . . . .                                   | 22         |
| 4.2 Horizontal current field around the STD site . . . . .                 | 29         |
| 4.3 The coastal and local wind field . . . . .                             | 30         |
| 4.4 Particle dispersion . . . . .  | 32         |
| 4.4.1 Sedimentation of particles . . . . .                                 | 32         |
| 4.4.2 Concentration of pelagic particles for scenarios S3 and S4 . . . . . | 33         |
| 4.4.3 Convergence of pelagic particles outside the disposal area . . . . . | 36         |
| <b>5 Discussion</b>  | <b>39</b>  |
| 5.1 Validation of the Førdefjord160 model . . . . .                        | 39         |
| 5.2 Dispersion of particles . . . . .                                      | 41         |
| <b>6 Conclusions</b>   | <b>45</b>  |
| 6.1 Outlook . . . . .  | 46         |

|   |           |
|---|-----------|
| <b>Bibliography</b>                           | <b>47</b> |
| <b>Appendix</b>                               | <b>53</b> |
| <b>A Moorings</b>                             | <b>55</b> |
| <b>B CTD stations</b>                         | <b>59</b> |
| <b>C Annual current field at the stations</b> | <b>61</b> |

# Chapter 1

## Introduction

Fjords in Norway have been the site of mine waste disposal since the late 17th Century (Ramirez-Llodra et al., 2015). Norway has the largest amount of Submarine Tailing Disposals (STDs) in the world, including seven active sites, 11 inactive, and two new sites accepted in 2018-2019 (Ramirez-Llodra et al., 2022, 2015). Tailing is the waste produced after extracting the targeted mineral, and STD is one of several methods for handling the waste from the mining industry (Ramirez-Llodra et al., 2015). One of the newly permitted sites is in Førdefjorden, which is an extensive debate in Norway. Major implications of STDs are for instance potentially toxic compounds within the tailing, smothering of the benthic infauna, and dispersion of the tailing in the fjord system (Ramirez-Llodra et al., 2015; Dold, 2014; Vare et al., 2018).

The circulation in fjords varies in terms of the topography, the proximity of coastal water, wind patterns, and the amount of freshwater runoff. The Norwegian fjords are usually long, narrow, and deep, with a sill at the fjord mouth accompanied by one or several basins towards the fjord head. The sill is a topographic barrier separating the fjord basin from the sea (Aksnes et al., 2019). The fjord mouth connects the fjord to the sea, and the head is the inland termination of the fjord (Farmer & Freeland, 1983). Rivers typically discharge in the fjord head area. Freshwater is less dense than seawater and forms a brackish surface layer. The freshwater input causes a stronger stratification in fjords relative to the adjacent coastal water. Horizontal pressure gradient forces induce baroclinic currents between the fjord and the coastal water (Inall & Gillibrand, 2010). This water exchange happens mainly between the surface layer and the sill depth, i.e. the intermediary layer (Asplin et al., 1999). The water below sill depth is called the basin water. The three-layering structure is a generic way of categorizing the different water masses in fjords (Figure 1.1) (Stigebrandt, 2012).

In fjords with relatively deep sills, the intermediary circulation is the dominating mechanism for coast-fjord water exchange (Aure et al., 1996). The intermediary water is situated between the sill depth and the surface layer, and thus the water is directly in contact with the coastal water (Figure 1.1). The coastal water consists of the Norwegian Coastal Current (NCC), which is a buoyancy-driven current flowing northwards along the Norwegian coast (Sætre, 2007a). The NCC is mainly driven by coastal wind and freshwater runoff from the Baltic Sea and fjords along the Norwegian southwest coast. On the seaward side and parallel to the coastal current flows the Norwegian Atlantic Current (NAC) (Figure 1.1). There is a dynamic interaction between the two currents, and mixing with the more saline NAC increases the salinity of the NCC and thus the stratification of the NCC decreases when travelling northwards (Sætre, 2007a). The NCC highly influences the intermediary circulation, and the density distribution

in this layer in fjords tends to mirror the density field at the coast (Aksnes et al., 2019).

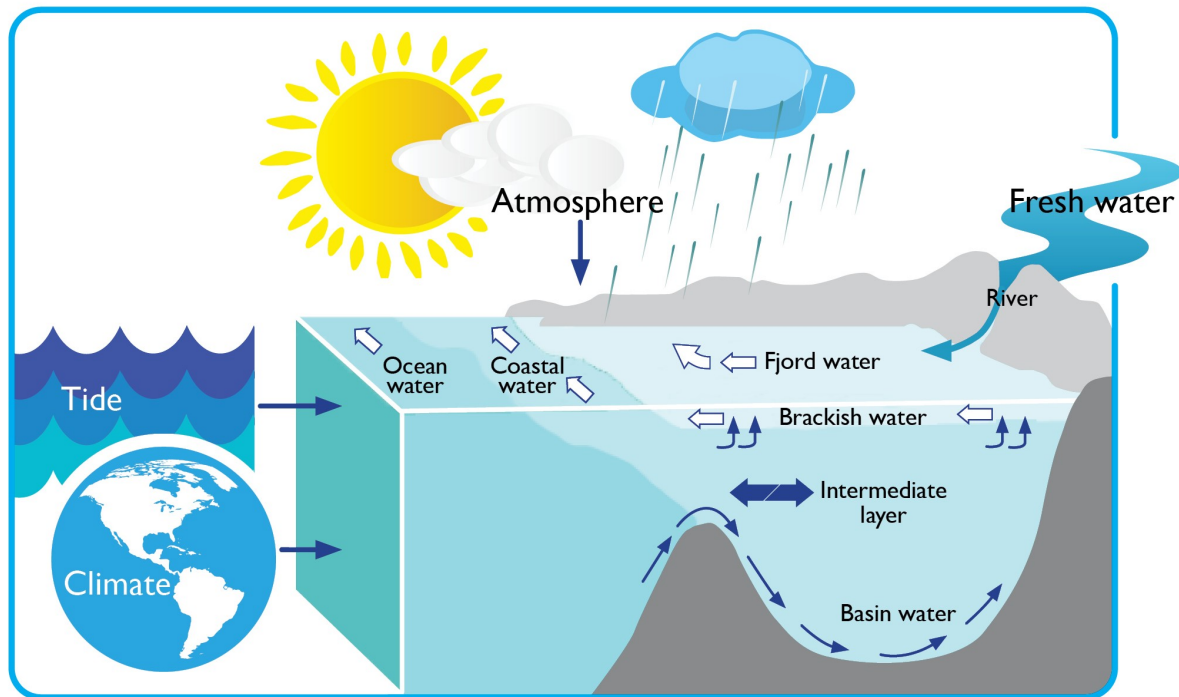


*Figure 1.1: Schematic of the typical structure of a Norwegian fjord and the main forcing mechanisms driving the fjord circulation. Source: Institute of Marine Research.*

The study of the intermediary circulation is limited in comparison with the estuarine circulation and tidal exchange (Farmer & Freeland, 1983; Aure et al., 1996; Arneborg, 2004). The crooked coastal topography largely influences the water exchange between the coast and the fjord and is likely a reason for the limited research on the topic (Asplin et al., 1999). A way to enhance the knowledge of the intermediary circulation in addition to obtaining more observations, is to apply models. Ocean models are used in an extensive range of applications, such as the physics of the global ocean, individual oceans, specific coastal regions, and fjords coupled to external components (Shchepetkin & McWilliams, 2009). These are for instance the atmosphere, river runoff, and seafloor sediments. The Institute of Marine Research (IMR), the Norwegian Meteorological Institute (MET Norway), and the Norwegian Institute of Water Research (NIVA) developed the coastal model Norkyst800 (Myksvoll et al., 2018). MET Norway runs the model operationally with daily forecasts (Dalsøren et al., 2020), and IMR runs an operational salmon lice model based on results from Norkyst800 (Asplin et al., 2020). The salmon lice model consists of the Lagrangian Advection and Diffusion Model (LADIM) (Ådlandsvik, 2022) that uses the hydrodynamic results from Norkyst800 to calculate particle trajectories (Asplin et al., 2020). MET Norway also developed a framework for trajectory modeling called OpenDrift (Dagestad et al., 2018). OpenDrift can be used to predict for instance oil drift, drifting objects for search and rescue, and microplastics in the ocean (Dagestad et al., 2018). The combination of hydrodynamic and trajectory modeling can also be used to investigate the dispersion of mine tailing.

The mining industry produces large amounts of waste both formed by non-processed rock from access tunnels and shafts and by processed tailing (Ramirez-Llodra et al., 2015). The tailing can be up to 99.99% of the ore, and it is usually stored in land-based dams. However, the potential risk of dam failure, rugged topography, and land availability in general lead to an increase in submarine disposal of mine tailing (Ramirez-Llodra et al., 2015). An additional advantage of STD is the prevention of acid drainage, since acids produced by sulfide oxidation are neutralized by the buffer capacity of seawater (Dold, 2014). Furthermore, there has been a major increase in the demand for minerals and metals over the last century due to both economic and world population growth (Vare et al., 2018; Dold, 2014). The increase in STD sites appears despite the lack of well-established techniques and practices for discharging mine tailings into the marine environment (Ramirez-Llodra et al., 2022). A better understanding of the dynamics at the STD site and tailing properties is needed to determine the spread of the tailing (Ramirez-Llodra et al., 2022).

The STD permitted in Førdefjorden is due to the production of titanium dioxide ( $\text{TiO}_2$ ) and garnet from the Engebø mountain adjacent to the fjord. Previous studies conducted in Førdefjorden are mainly impact assessments regarding the planned STD. The impact assessment by Staalstrøm & Molvær (2009) describes the process from extracting the targeted minerals from the ore to the disposal of the remaining tailing. The ore is grained down to grain sizes of  $< 0.3 \text{ mm}$  before the minerals are extracted. The tailing is fine-grained at this stage and is flocculated to increase the sinking velocity when discharged into the fjord (Staalstrøm & Molvær, 2009). The flocculation process reduces the amount of fine-grained particles to  $5 \times 10^{-3} \%$  of the tailing (Vogelsang & Bjerkeng, 2014). This fine fraction has a low sinking velocity and nearly does not settle at the fjord bottom (Staalstrøm & Molvær, 2009). The amount of fine fraction is uncertain, and the impact assessments have mainly focused on investigating the impact of larger particles (Nepstad & Rye, 2014). Staalstrøm & Molvær (2009) include the fine fraction, but the report investigates a potential accident where particles are discharged at the surface for seven days only. Ramirez-Llodra et al. (2022) report that the most fine-grained particles of the tailing have the most profound effect on the benthic infauna, which is the organisms living within the sediments on the seafloor. Furthermore, Rygg (2007) investigates the benthic infauna in Førdefjorden, and finds that the fjord has a rich infauna compared to other western Norwegian fjords. Despite these findings, the knowledge of how the fine-grained particles can potentially disperse in Førdefjorden is limited.

In my thesis, I will investigate the dispersion of the fine fraction of the mine tailing in Førdefjorden. I assume that 1% of the fine fraction of the total mine tailing is left after the flocculation process. The fine fraction contains particles with a grain size of  $< 15 \mu\text{m}$ . Table 1.1 contains the regulations regarding the permitted STD that I consider in my thesis (Anon., 2023). I additionally set the annual tailing discharge to  $4 \times 10^9 \text{ kg yr}^{-1}$ , which is the maximum permitted amount of mine tailing. This gives an annual amount of fine fraction of  $4 \times 10^7 \text{ kg yr}^{-1}$ .

*Table 1.1: Regulations for the permitted STD in Førdefjorden (Anon., 2023). RD stands for release depth of particles.*

|   |                          |
|---|--------------------------|
| Sedimentation                           | $3.0 \text{ mm yr}^{-1}$ |
| Concentration 40 m above RD             | $2.0 \text{ mg l}^{-1}$  |
| Concentration outside STD area below RD | $3.0 \text{ mg l}^{-1}$  |

The objective of my thesis is to study future scenarios of particle dispersion in Førdefjorden. I investigate how the fine fraction disperses with varying particle release depth and the bathymetry in the fjord. I use results from a hydrodynamic fjord model to look at the circulation in Førdefjorden. The model is run twice for the same period with two different bathymetries. I examine the transport of particles by applying a particle tracking model, where I vary the release depths. Additionally, I use hydrographic and current observations conducted by IMR to evaluate the fjord model performance. I aim to investigate the following research questions:

- Does the hydrodynamic model simulate realistic circulation in Førdefjorden in comparison with observations?
- How do changes in bathymetry and release depth of particles affect the particle dispersion in the fjord?
- Will the dispersion of the fine fraction be pronounced in regard to the regulations?

The structure of this thesis is as follows: Chapter 2 includes background theory about fjord dynamics. Chapter 3 contains a presentation of the study area, the models and the data I use, the setup of the scenarios, and relevant equations. Furthermore, I present the results from model validation and particle dispersion in Chapter 4. I discuss my findings in Chapter 5, followed by a conclusion and future perspectives in Chapter 6.

# Chapter 2

## Background

### 2.1 Coast-fjord water exchange

The main forcings of water exchange between fjords and the coast are freshwater runoff, wind, horizontal pressure gradients, and tides (Asplin et al., 2020). Figure 2.1 illustrates the common circulation patterns in fjords. The estuarine circulation is situated in the surface layer and is mainly driven by freshwater runoff from rivers discharging in fjords (Myksvoll et al., 2011). The input of freshwater generates a higher pressure of the surface layer inside the fjord than outside, inducing a current propagating out of the fjord (Stigebrandt, 2012). Local winds in fjords are typically steered by the surrounding topography and are thus primarily directed along the fjord axis. The wind and tides induce mixing between the fresher surface layer and the more saline water beneath and form a brackish surface layer (Aure et al., 2007). In the absence of freshwater input, the brackish layer is non-existent. Additionally, the brackish layer might not be present in the outer part of long fjords due to mixing processes (Asplin et al., 2020). The main sources of mixing in the surface layer are current shear and wind (Dyer, 1997). The coast-fjord water exchange due to the estuarine circulation is relatively small in comparison with other water exchange components (Aure et al., 2007).

The effect of wind on fjord circulation can be divided into local and non-local wind forcing (Asplin et al., 1999). While the local wind pushes the surface water with a mechanical drag and generates mixing (Aure et al., 2007), the non-local wind forcing concerns the influence of coastal winds on the fjord circulation. Norway is located in the path of the atmospheric polar front which regularly sends low-pressure systems towards the coast (Asplin et al., 2020). This leads to episodically strong coastal winds at the Norwegian west coast with a duration typically less than a day. Although the direction changes from the angle of the eastward propagating atmospheric lows, it is typically more southerly winds during winter and northerly winds during the summer. The southerly wind will lead to a convergence of water towards the coast (Ekman transport; Cushman-Roisin & Beckers, 2011). The convergence results in downwelling of lighter surface water downstream of the fjord mouth. The downwelling generates an internal Kelvin wave subsequently propagating into the fjord. The depressed phase of such a wave will have a corresponding current in the upper layer in the direction of the wave propagation, i.e. into the fjord. Below the upper layer flows an opposite directed current scaled so the vertically integrated current in the whole water column is zero. Northerly wind will cause a divergence of water towards the coast. Divergence of water leads to upwelling, which is the process of denser water being lifted outside the fjord mouth. A similar internal Kelvin wave is generated but in the elevated phase. The corresponding current in the upper layer will be in the opposite

direction of the wave propagation, i.e. out of the fjord (Asplin et al., 1999).

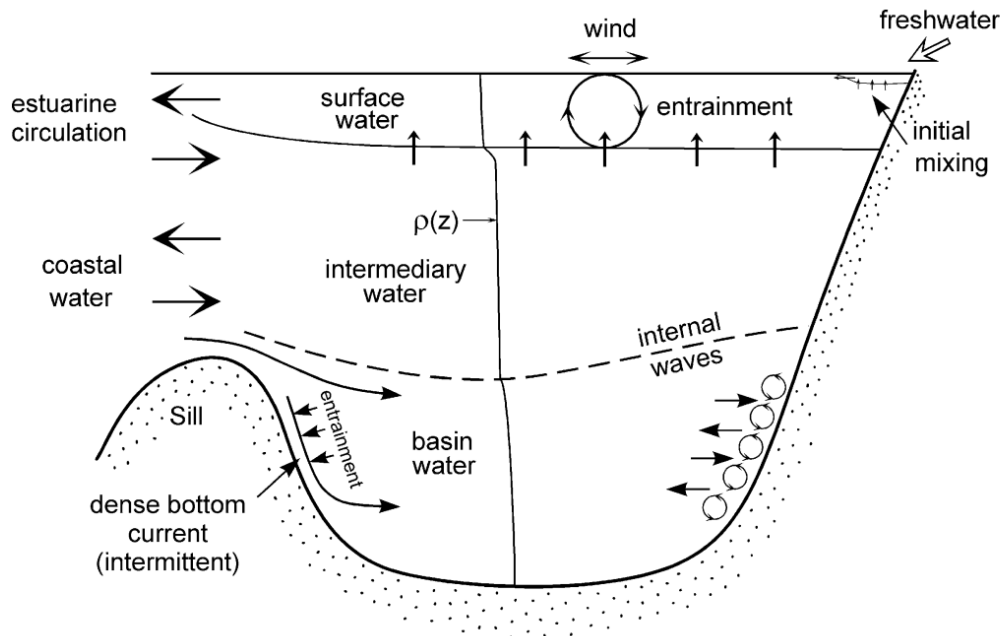


Figure 2.1: The different water masses in a deep silled fjord, and processes happening within and between the layers. Figure from Stigebrandt (2012).

Coastal upwelling and downwelling are important features of the coast-fjord water exchange (Sætre, 2007b). During upwelling at the coast, denser water can get lifted above sill depths and can potentially enter the fjords (Asplin et al., 1999). If the entraining coastal water is sufficiently dense, it can sink deeper than the sill depth replacing parts of the basin water. These inflow events of dense coastal water replacing the basin water in the fjord are termed deep water renewals. The inflows are often intermittent, which can result in a partial renewal (Gade & Edwards, 1980). Another factor that might reduce a renewal episode is mixing between the entraining coastal water and the resident basin water. The mixing reduces the density of the inflow, such that the inflow of water does not reach the bottom of the basin (Figure 2.1) (Gade & Edwards, 1980).

Another important forcing on fjord circulation is tides. The tide propagates from south to north along the Norwegian coast as a Kelvin wave and the M2 constituent is the leading mode (Asplin et al., 2020). Tides feed energy to fjords through internal waves and jets. The tide propagates into the fjord as a barotropic wave, and the influence of topography and the stratification in the fjord can generate internal waves, which again can induce turbulence and diapycnal mixing processes in the fjord (Farmer & Freeland, 1983; Stigebrandt, 2012). In fjords with shallow and narrow sills, the currents due to tides are energetic and cause mixing at the sill (Tinis & Pond, 2001). In wide and deep fjords, the current speed due to tides is modest (Asplin et al., 2020), but the influence of tides on mixing in the basin is still important.

## 2.2 Rotational dynamics

Fjords can be classified as narrow or broad by comparing the fjord width  $L$  to the internal radius of deformation  $R_i$  (the Rossby radius). A fjord is narrow if  $L < R_i$  and broad if  $L > R_i$ . The effect of Earth's rotation on the fjord circulation becomes important in broad fjords (Cushman-Roisin et al., 1994).  $R_i$  in a two-layered fjord is defined as

$$R_i = \frac{c_i}{f} \quad (2.1)$$

where  $f$  is the coriolis parameter and  $c_i$  is the internal wave speed given by

$$c_i^2 = \frac{g'H_1H_2}{H_1 + H_2} \quad (2.2)$$

$H_1$  and  $H_2$  are the thicknesses of the upper and lower layers, respectively.  $g'$  is the reduced gravity defined as

$$g' = \frac{g(\rho_2 - \rho_1)}{\rho_2} \quad (2.3)$$

$\rho_1$  and  $\rho_2$  are the densities of the layers, and  $g$  is the gravitational acceleration.  $R_i$  depends on the stratification of the fjord, which is typically highest in the upper part of the fjord and decreases with depth. Thus,  $R_i$  will decrease with increasing depth, i.e. the influence of rotation can become more important for the dynamics at depth.



# Chapter 3

## Material and methods

In this chapter, I will present the study area of Førdefjorden, the models and the datasets I use to investigate the dynamics and particle dispersion in Førdefjorden. The datasets include modeled and observed oceanic data provided by IMR, in addition to modeled atmospheric data from MET Norway. Furthermore, I will describe my experiments and briefly explain the instruments used to sample the data. Lastly, I will present the equations I use to calculate my results.

### 3.1 Study Area

Førdefjorden is located at the western coast of Norway at  $61.5^{\circ}\text{N}$  and  $5.5^{\circ}\text{E}$  (Figure 3.1a). The fjord is 75 km long and is divided into an inner and outer part by a 55 m deep sill at Ålasundet (Figure 3.1c) (Staalstrøm & Daae, 2009). The inner part of the fjord is deepest close to Ålasundet with depths down to 350-400 m, and becomes shallower towards the head of the fjord. There are two major rivers discharging into the inner part of Førdefjorden, named Jølstra and Nausta (Bruvold et al., 2023). Jølstra has its outlet at the fjord head by the town Førde, while Nausta runs out in the fjord by the village Naustdal 10 km west of Førde. The rivers are national salmon rivers, and the inner part of Førdefjorden is therefore a national salmon fjord (Kögel, 2019). The outer part of the fjord is about 300 m deep at the planned STD site, which is marked by the black dashed lines in Figure 3.1c. The STD area extends westwards into a deeper basin of depths down to 340 m. There is a deep sill at approximately 305 m depth separating the two basins in the outer part of the fjord (Staalstrøm & Daae, 2009). The outer basin is deepest by Flokeneset with depths down to 375 m. There are additionally two sills further out westwards towards the coast. The southern sill between Flokeneset and Svanøy is 20 m deep, and the northern sill between Svanøy and Skjeljevikneset is at 210 m depth, with respective widths of 3.7 and 2.5 km. The fjord width ranges from 2.9 km to a couple of hundred meters. The surrounding topography is mountainous with heights up to 1304 m. In this project, however, I will focus mainly on the area enclosed by the red rectangle in Figure 3.1b and shown in Figure 3.1(c,d).

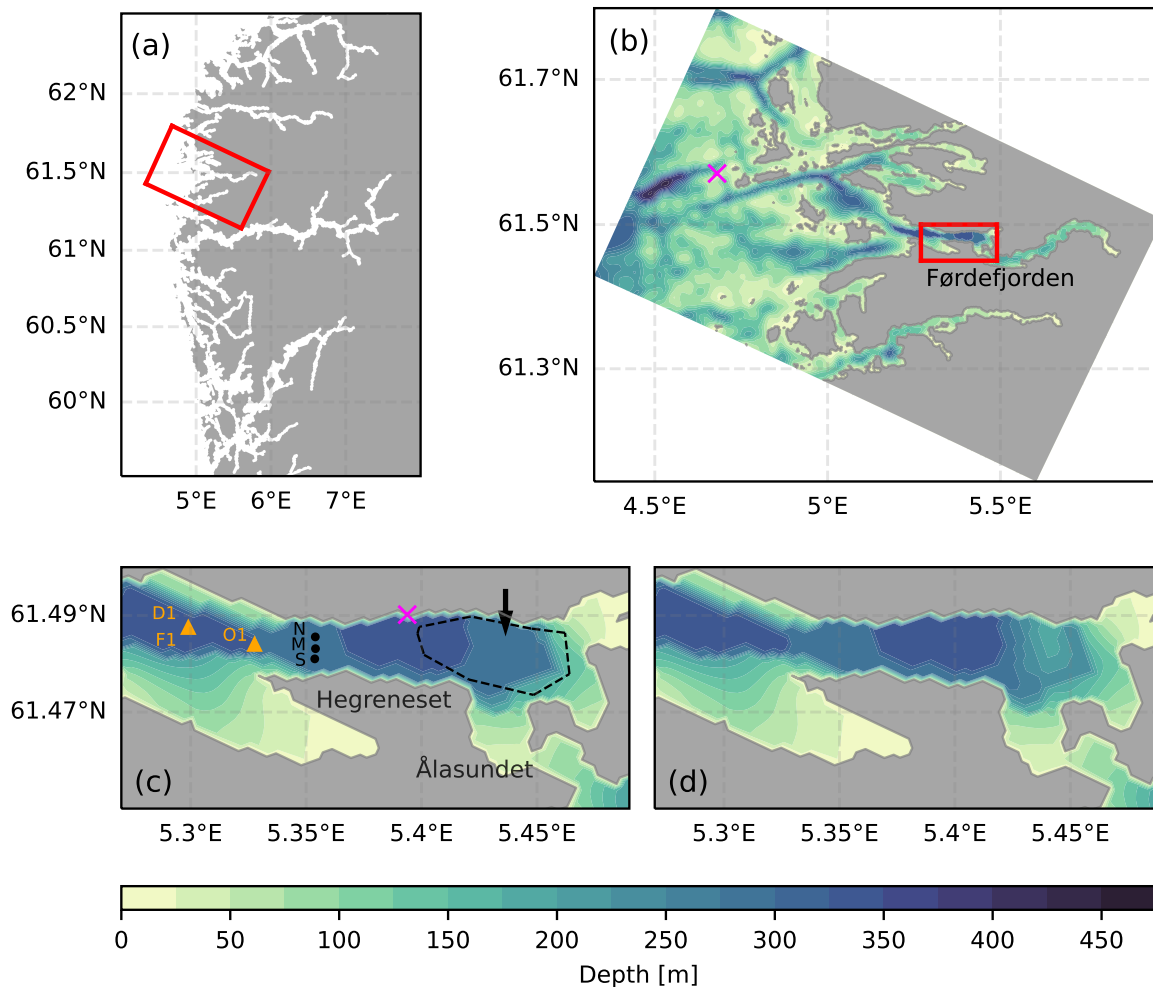


Figure 3.1: Maps of the study area showing the location of the Fjørdefjord160 model domain at the western coast of Norway (a), and the Fjørdefjord160 model domain including the model bathymetry (b). The red rectangle in (b) encloses the area shown in the lower panels (c,d). (c) includes the release point of particles for the LADIM runs (black arrow), and the black dashed lines illustrate the planned STD site based on an estimation done by Asplan Viak (Anon., 2014). The black dots show the location of the current measurement stations and the orange triangles display the location of the CTD stations. The pink crosses show the wind data locations at Ytreøyane (b) and Vevring (c). (d) displays the modified bathymetry in the STD area used for future scenarios. Land contours from Norkyst800 (a) and Fjørdefjord160 (b,d,c).

## 3.2 Hydrodynamic fjord model

I used output data from the hydrodynamic fjord model Fjørdefjord160 to examine the dynamics in Fjørdefjorden. Fjørdefjord160 is a high-resolution model based on the open-source Regional Ocean Modeling System (ROMS, <https://www.myroms.org>), with a horizontal resolution of  $160\text{ m} \times 160\text{ m}$  and with 35 vertical levels. ROMS is a state-of-the-art, three-dimensional, free surface, hydrostatic, primitive equation model that uses generalized terrain-following sigma coordinates in the vertical (Haidvogel et al., 2008; Shchepetkin & McWilliams, 2005).

The hydrodynamic boundary forcing along the open boundaries of Fjørdefjord-160 is from the

fjord model Norfjords160 which again gets boundary values from the coastal model Norkyst800. Norkyst800 covers the Norwegian coast with  $800 \text{ m} \times 800 \text{ m}$  horizontal resolution and also implements ROMS (Albretsen et al., 2011). IMR established Norkyst800 to estimate salmon lice dispersion along the Norwegian coast, but it has great general applicability (Asplin et al., 2020). To study fjords with narrow sounds and crooked topography, IMR developed Norfjords160 parallel to Norkyst800 (Albretsen & Asplin, 2021). Norfjords160 covers the Norwegian coast in 13 subareas with  $160 \text{ m} \times 160 \text{ m}$  horizontal resolution (Asplin et al., 2020). The horizontal resolution is the only difference between the models. Førdefjord160 is a modification of Norfjords160. The subarea A05 of Norfjords160 covers "Sogn og Fjordane" including Førdefjorden. Førdefjord160 has a smaller model domain to speed up the simulation, but also a more realistic bottom matrix than the A05. The results from Førdefjord160 and Norfjords160 are comparable.

The model domain of Førdefjord160 covers Førdefjorden and the surrounding area from Dalsfjorden in the south to the southern part of Frøyssjøen in the north. The grid is rotated with an angle of approximately  $65^\circ$  relative to the longitude, which is visible in Figure 3.1(a,b), and it is divided into  $281 \times 471$  grid cells. The vertical resolution is highest in the surface layer and decreases with depth with a small increase again in the lowest layers. The model was run twice from July 2021 to June 2022. The first run included a bottom matrix representing the present bathymetry, while the second run had a bathymetry simulating modifications caused by tail deposits. This is explained further in Section 3.3.1.

Førdefjord160 takes hourly data from parts of a 25-year hindcast archive of Norkyst800 results (Dalsøren et al., 2020; Asplin et al., 2020). The atmospheric forcing in Førdefjord160 is from the weather prediction model AROME-MetCoOp (Meteorological Co-operation on Operational Numerical Weather Prediction) 2.5 km, which is the main forecasting system at MET Norway (Müller et al., 2017). Tidal forcing is from TPXO7.2 global tidal analysis (Egbert & Erofeeva, 2002; Dalsøren et al., 2020). Daily river flow rates are included based on estimates of runoff in all catchment areas in Norway provided by the Norwegian Water Resources and Energy Directorate (NVE). Further details about model configurations can be found in Dalsøren et al. (2020), which describe the model setup for Norfjords160.

### 3.3 Particle tracking model

To examine the particle drift, I used the Lagrangian Advection and Diffusion Model (LADIM) developed at IMR (Ådlandsvik & Sundby, 1994; Ådlandsvik, 2022). LADIM is an offline ocean particle tracking model and it takes input data from ROMS (Ådlandsvik, 2022). In my experiments, the model is forced with the current output from Førdefjord160. LADIM calculates the velocity at a given location by using bilinear interpolation. To transport the particles, LADIM uses the Runge-Kutta fourth-order method (Boyce & DiPrima, 2005). The model is set to release one super particle per minute at a given release depth, and the output is per day as a snapshot. One super particle represents the mass of 76 kg of particles. The maximum age of a particle is 40 days. If a particle does not settle after 40 days, it is discarded from the simulation to reduce the computational demand. The vertical and horizontal mixing are set to constant values of  $10^{-5} \text{ m}^2 \text{ s}^{-1}$  and  $0.1 \text{ m}^2 \text{ s}^{-1}$  respectively.

### 3.3.1 Setup for the scenarios

In my particle tracking experiments, I vary between two different model bathymetries and four release depths. I ran LADIM for one year for each scenario equivalent to the simulation period for F rdefjord160. Table 3.1 shows the setup for the different runs. Scenario S1 has a release depth of particles at 280 m depth and a bathymetry representing the present bathymetry in the fjord. Scenario S2 also includes the present bathymetry but the release depth is set to 250 m depth. The future scenarios S3 and S4 have release depths of particles at 150 and 100 m depth, respectively, and include a modified bathymetry. The modified bathymetry is an assumption based on the estimation by Omholt et al. (2014) of the basin bottom after 50 years of tailing disposal. The pipe discharging the tailing is assumed to move upwards with time only, creating a mountain-like structure (Figure 3.1d). The particles are released at 61.495 N and 5.436 E, shown by the arrow in Figure 3.1c. The grain size was set to  $< 15\mu\text{m}$ . The corresponding sinking velocities  $v$  can be calculated using Stokes law:

$$v = \frac{2}{9} \frac{(\rho_p - \rho_f)}{\mu} g R^2 \quad (3.1)$$

$\rho_p$  is the density of the particle,  $\rho_f$  is the density of the fluid,  $\mu$  is the dynamic viscosity,  $g$  is the gravitational acceleration, and  $R$  is the radius of the spherical particle. Particles with size  $< 15\mu\text{m}$  will sink with a velocity of  $< 2 \times 10^{-4} \text{ms}^{-1}$ . The sinking velocity is set to  $10^{-4} \text{ms}^{-1}$  in all scenarios as a representative mean value.

*Table 3.1: Setup for the different scenarios.*

| Scenario | Release depth [m] | Bathymetry |
|----------|-------------------|------------|
| S1       | 280               | Present    |
| S2       | 250               | Present    |
| S3       | 150               | Modified   |
| S4       | 100               | Modified   |

## 3.4 Measurements

### 3.4.1 Current measurements

IMR deployed three acoustic doppler current profilers (ADCP) across F rdefjorden to measure the current in the fjord from February to May 2022. The ADCPs were of the type Nortek Signature 250 and were located in three positions across the fjord to the west of the planned STD area (Figure 3.1c). They were anchored at the bottom and measured from 283 m and 251 m depending on the bottom depth. Table 3.2 contains further information about the station locations and sampling range. Figure 3.2 shows a schematic of the mooring setup at the northern position. Schematics of the middle and southern moorings are in Appendix A (Figures A.1 and A.2).

The instrument measures current velocity by emitting sound signals in four beams from transducers, which are reflected by particles in the water and received again by the transducers. The instrument then calculates the velocity with the following equation:

$$V = \frac{F_{\text{Doppler}}}{F_{\text{Source}}} \cdot \frac{c}{2} \quad (3.2)$$

$V$  is the velocity in the direction of the sound signal,  $F_{\text{Doppler}}$  is the change in frequency of the received signal (the Doppler shift),  $F_{\text{Source}}$  is the frequency of the emitted wave, and  $c$  is the speed of sound (Nordek, 2018). The sampling area is divided into vertical grid cells and the calculated velocities are averaged within every cell. The cell size for this experiment was set to 4 m. The sampling interval was 20 minutes, with an averaging interval of 100 seconds per sampling. The accuracy of Signature250 can be found in Table 3.3.

Table 3.2: Properties of the current observation stations.

| St. | Lat [°N] | Lon [°E] | Deployment time | Recovery time  | Bottom depth [m] | Sampling range [m] |
|-----|----------|----------|-----------------|----------------|------------------|--------------------|
| N   | 61.486   | 5.354    | 17.02.22 23:30  | 31.05.22 22:30 | 343              | 283-109            |
| M   | 61.483   | 5.354    | 17.02.22 23:35  | 07.05.22 09:35 | 344              | 283-109            |
| S   | 61.481   | 5.354    | 17.02.22 23:40  | 07.05.22 09:00 | 311              | 251-77             |

### 3.4.2 Hydrographic measurements

IMR has hydrographic data from Førdefjorden from nine different years. The hydrographic data is from CTD stations, and the location of stations and in which months the stations are taken varies each year. I chose CTD stations from within the model simulation period and from around the STD area marked as orange triangles in Figure 3.1(c). The profiles are from October 2021, December 2021, and February 2022. The stations are named after which month they are sampled. Table B.1 contains detailed information about locations, dates, and depths of profiles. The instrument used at all stations was an SBE 911plus CTD, and the accuracy of the different sensors is listed in Table 3.3. The instrument measures temperature, conductivity, and pressure, and calculates salinity from the obtained measurements.

Table 3.3: Accuracy of the current profiler signature250 and SBE 911plus CTD.

| Instrument   | Sensor       | Accuracy   |
|--------------|--------------|--|
| Signature250 | Velocity     | 1.0% of measured value $\pm 5.0 \times 10^{-4} \text{ m s}^{-1}$ |
|              | Direction    | 2.0° for tilt $< 30.0^\circ$                                     |
| SBE 911plus  | Conductivity | $3.0 \times 10^{-4} \text{ S m}^{-1}$                            |
|              | Temperature  | $1.0 \times 10^{-3} \text{ }^\circ\text{C}$                      |
|              | Pressure     | $1.5 \times 10^{-2} \text{ \% full scale}$                       |

## 3.5 Wind data

I include local wind in Førdefjorden and coastal wind from outside Førdefjorden to investigate how it influences the water exchange in the fjord. The wind data is from the weather prediction model AROME-MetCoOp (Müller et al., 2017), which also provides the atmospheric

forcing in the Førdefjord160 model. The data is available online at thredds.met.no. AROME-MetCoOp has a horizontal resolution of  $2.5 \text{ km} \times 2.5 \text{ km}$  and covers large parts of the Nordic countries, including the North Sea, the Baltic Sea, and parts of the Atlantic Ocean (Müller et al., 2017). The wind data I use is wind speed interpolated to 10 m height. The coastal wind is from Ytreøyane and the local wind is from Vevring, both locations shown as pink crosses in Figure 3.1(b,c).

### 3.6 Sedimentation and concentration calculations

LADIM does not calculate the sedimentation and concentration of particles, but it calculates the annual settlement and the daily drift of particles. Thus, I count the settled particles in each grid cell and use Equation 3.3 to calculate the sedimentation. For the concentration calculations, I count particles in the grid from the daily output and further calculate the concentrations using Equation 3.5.

The annual sedimentation  $s$  of particles in the grid can be obtained by using the following equation:

$$s = n_{ps}s_p \quad (3.3)$$

where  $n_{ps}$  is the number of settled particles in each grid cell. The sedimentation of one particle  $s_p$  is given by

$$s_p = \frac{1000m_p}{\rho_s} \quad (3.4)$$

where  $m_p = m_f/(n_{tot}A)$  is the mass of one particle per  $\text{m}^2$  in a grid cell. The mass of the fine fraction  $m_f$  is defined as 1% of the total tailings,  $n_{tot}$  is the number of settled particles in the grid, and  $A = 160 \text{ m} \times 160 \text{ m}$  is the area of a grid cell.  $\rho_s = 2760 \text{ kg m}^{-3}$  is the density of the sediment including 25% freshwater.

The daily concentration  $C$  of particles can be expressed as

$$C = \frac{m n_p}{V} \quad (3.5)$$

where  $n_p$  is the number of particles in each grid cell,  $m$  is the mass of a particle, and  $V$  is the volume of a grid cell with a vertical bin size of 10 m. Thus,  $V = 160 \text{ m} \times 160 \text{ m} \times 10 \text{ m}$ . The mass of a particle is given by

$$m = \frac{q_m}{n_s}, \quad (3.6)$$

where  $n_s = 1/60 \text{ s}^{-1}$  is the amount of particles released per second, and  $q_m$  is the mass flux of particles.

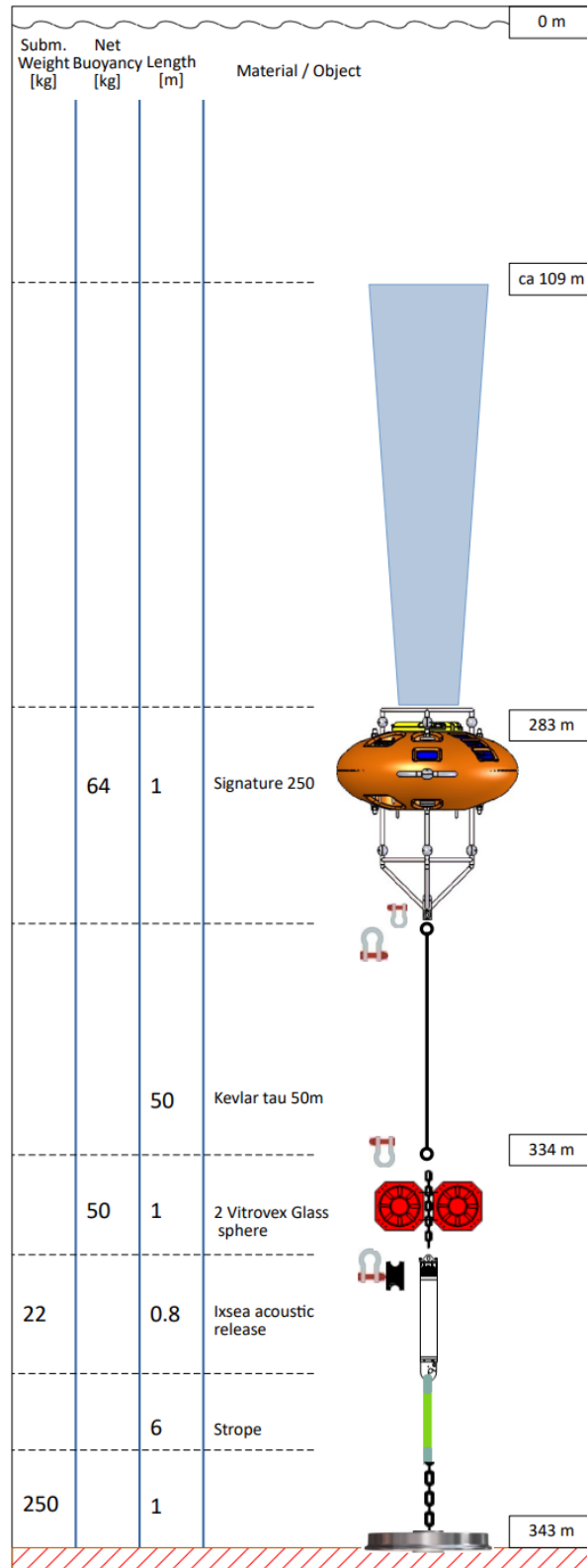


Figure 3.2: Schematic of the moored instruments at the northern position in Førdefjorden. Source: IMR.



# Chapter 4

## Results

In this chapter, I will present the results from the model validation of Førdefjord160, followed by a comparison of the modeled current field with the present and the modified bathymetry. Furthermore, I will present the coastal wind field outside Førdefjorden and the local wind field in the fjord. Lastly, I present the results from the particle dispersion scenarios both in the pelagic phase and the settlement of the particles. In this last section, I also investigate an event of convergence of pelagic particles. The data included in this chapter is either from the period of current observations or from the whole simulation period for the Førdefjord160 model. The former is from the 18th of February to the 31st of May 2022, and the latter is from the 1st of July 2021 to the 30th of June 2022.

### 4.1 Validation of Førdefjord160

This section contains a comparison of the modeled and the observed hydrography field, and of the modeled and observed current field. How the model resolves the current field is crucial to further examine the transport of particles. Thus, I focus mainly on validating the current field.

#### 4.1.1 Hydrography

Figure 4.1 presents the modeled salinity (a) and temperature (b) per hour for the simulation period together with observations shown as dots in the figure. Values below 30.0 PSU are colored black (Figure 4.1a). The profiles displayed in Figure 4.2 correspond to the observations in Figure 4.1. The model grid point I use in the figures has the same location as the CTD stations taken in December 2021 and February 2022, shown as D1 and F1 in Figure 3.1c. The CTD station from October 2021 is located slightly east of the two other stations. Table 4.1 contains corresponding minimum, maximum, mean, and standard deviation estimates of the observed and simulated salinity and temperature, and also of the model for the total period.

The modeled salinity and temperature fields show a seasonal pattern during the year, and a high variability in the upper 100 m (Figure 4.1). In July 2021, there is a fresh and warm surface layer. The surface layer becomes shallower, cooler, and more fresh in September. From October to the end of November there is a freshening of the whole water column with a corresponding increase in temperature. The observations in October and December do not show the same change in depth, but the upper 75 m looks more similar to the observations (Figure 4.1). The simulated temperature field in January and February is mostly homogeneous below the surface layer (Figure 4.1b). The salinity field varies more during this period, and becomes

more homogeneous in March (Figure 4.1a). The surface layer becomes relatively shallow in April until it deepens during May and June with an increase in temperature and a decrease in salinity.

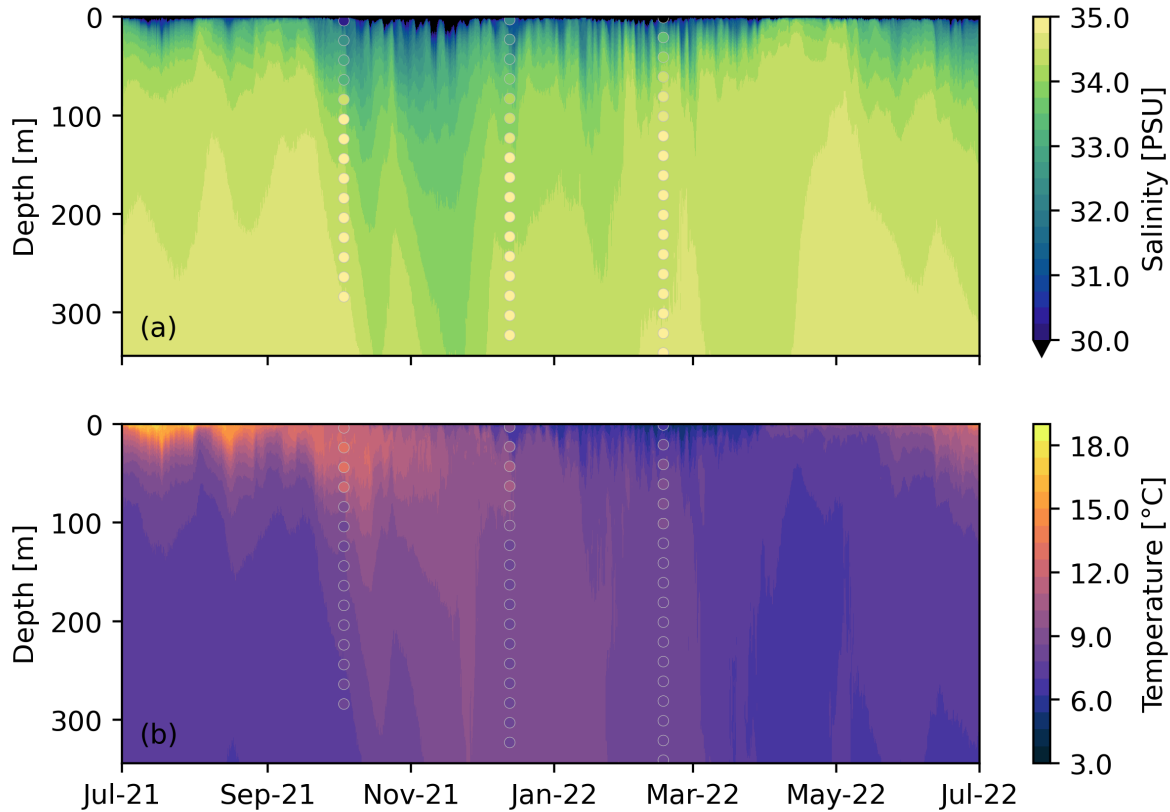


Figure 4.1: Simulated salinity (a) and temperature (b) for the total simulation period. The dots are the observed salinity and temperature from CTD stations taken on the 3rd of October 2021, the 13th of December 2021, and the 16th of February 2022.

Figure 4.2 show the observed and simulated profiles of salinity and temperature from October 2021 (a), December 2021 (b), and February 2022 (c). The profiles were sampled on the 3rd of October, the 13th of December, and the 16th of February. I extracted the modeled data from the same occasions. The dashed lines present the observed data, and the solid lines present the simulated data.

The observations in October show a distinct layer of warmer and fresher water right beneath the surface, and a colder and more saline layer from approximately 100 m depth and down to the bottom (Figure 4.2a). There is a clear thermo- and halocline separating the two layers. Within the bottom layer, the temperature reaches a minimum value of  $7.9^{\circ}\text{C}$  and the salinity has a maximum value of 35.1 PSU (Table 4.1). This layering is not captured by the model. The modeled salinity and temperature have a rapid increase at the surface, especially the salinity. The modeled temperature is constant for the next  $\sim 10$  m before it decreases towards the bottom to a minimum temperature of  $7.4^{\circ}\text{C}$ , while the simulated salinity gradually increases from below the rapid increase at the surface reaching a maximum salinity of 34.6 PSU (Figure 4.2a).

The upper 50 m of the simulated and observed temperature profiles in December are similar,

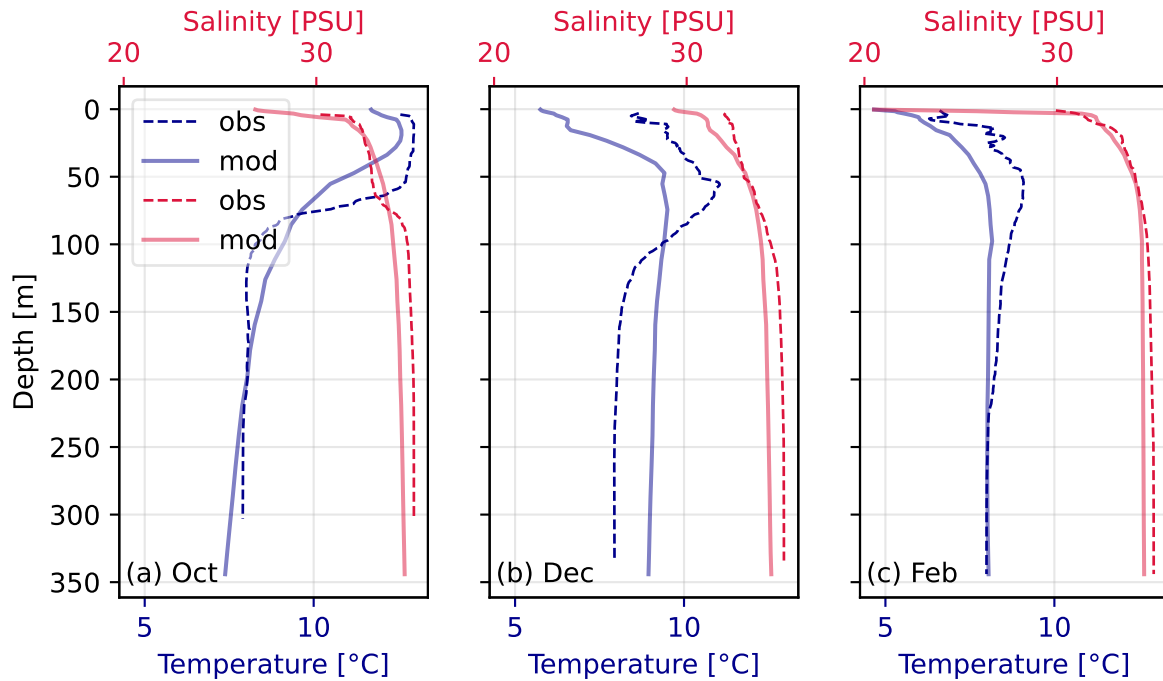


Figure 4.2: Simulated and observed temperature and salinity from the 3rd of October 2021, the 13th of December 2021 (b), and the 16th of February 2022 (c). The solid lines are modeled data, and the dashed lines are observed data.

except for the warm bias in the model (Figure 4.2b). There is a thin layer of constant temperature at  $\sim 10$  m depth both in the observations and the modeled temperature. The observed temperature reaches a maximum temperature of  $11.1^{\circ}\text{C}$  at approximately 50 m depth, decreases between 50 and 150 m depth, and is further constant with depth. The simulated temperature reaches a maximum temperature of  $9.5^{\circ}\text{C}$  at 75 m depth and is approximately constant below this depth (Figure 4.2b). The observed and simulated salinity are relatively similar, despite the fresher surface in the model and an additional fresh bias below 100 m depth. The maximum observed salinity is 35.1 PSU and the maximum modeled salinity is 34.4 PSU.

In February, the model has a minimum value in salinity of 20.5 PSU at the surface, which is 9.4 PSU less than the observed salinity at the surface (Figure 4.2c and Table 4.1). Despite this discrepancy at the surface, the salinity profiles look similar with maximum values of 34.5 PSU in the model and 35.0 PSU in the observations. The simulated temperature profile increases from  $4.7^{\circ}\text{C}$  in the surface to  $8.1^{\circ}\text{C}$  at 100 m depth, and is nearly constant below 100 m depth (Figure 4.2c). The observed temperature varies in the upper 50 m, reaching a maximum temperature of  $9.1^{\circ}\text{C}$  at approximately 50 m depth, and decreases again with depth. The observed and simulated temperatures are alike from 250 m to 350 m depth.

The model is cooler and fresher than the observations at the surface in each profile (Figure 4.2). This discrepancy is also evident in the minimum, maximum, and mean values in Table 4.1, except for a higher mean temperature in October. Considering the mean salinity values, the model is biased with 1.9 PSU in October, and with 1.8 and 2.0 PSU in December and February, respectively. The standard deviation of the modeled salinity is also greater than the standard deviation of the observed salinity. The modeled and observed mean temperatures correspond better (Table 4.1).

Table 4.1: The minimum, maximum, mean, and standard deviation of salinity (upper panel) and temperature (lower panel) from the model and CTD-stations as shown in Figure 4.2. The minimum, maximum, mean, and standard deviation of salinity and temperature for the total simulation period are also included.

|             | Min [PSU] |      | Max [PSU] |      | Mean [PSU] |      | Std [PSU] |     |
|-------------|-----------|------|-----------|------|------------|------|-----------|-----|
|             | MOD       | OBS  | MOD       | OBS  | MOD        | OBS  | MOD       | OBS |
| Oct         | 26.8      | 30.2 | 34.6      | 35.1 | 32.5       | 34.4 | 2.4       | 1.0 |
| Dec         | 29.3      | 32.0 | 34.4      | 35.1 | 32.6       | 34.4 | 1.7       | 0.9 |
| Feb         | 20.5      | 29.9 | 34.5      | 35.0 | 32.6       | 34.6 | 3.3       | 0.8 |
| Tot. period | 9.1       |      | 34.7      |      | 32.7       |      | 3.0       |     |

|             | Min [°C] |     | Max [°C] |      | Mean [°C] |     | Std [°C] |     |
|-------------|----------|-----|----------|------|-----------|-----|----------|-----|
|             | MOD      | OBS | MOD      | OBS  | MOD       | OBS | MOD      | OBS |
| Oct         | 7.4      | 7.9 | 12.6     | 13.0 | 10.2      | 9.2 | 2.0      | 2.0 |
| Dec         | 5.8      | 8.0 | 9.5      | 11.1 | 8.1       | 8.6 | 1.3      | 1.0 |
| Feb         | 4.7      | 6.6 | 8.1      | 9.1  | 7.2       | 8.3 | 1.1      | 0.4 |
| Tot. period | 3.0      |     | 19.4     |      | 8.7       |     | 2.2      |     |

#### 4.1.2 Selecting grid points for current field validation

To validate the model performance of simulating the current field in Førdefjorden, I chose three grid points in the model geographically close to the current measurement stations. I compared the mean, standard deviation, and extreme values of the stations with nine grid points around each station. From that, I selected the three grid points in Table 4.2. Since processes in the model can be shifted compared to observations, I additionally calculated the correlation between each station and a subarea from around the stations to look at how the model varies horizontally. Throughout the validation of the current field resolved by the model, I examine the period of the current observations which is from February to May 2022.

Table 4.2: The current measurement stations (Figure 3.1c) and the corresponding model grid points used in the validation.

| Station | Grid point ( $eta_{rho}, xi_{rho}$ ) | Lat [°N] | Lon [°E] |
|---------|--------------------------------------|----------|----------|
| N       | (177,179)                            | 61.486   | 5.355    |
| M       | (176,177)                            | 61.483   | 5.355    |
| S       | (176,174)                            | 61.479   | 5.351    |

The correlation between two variables gives a correlation coefficient  $r$  as a measure of how well the variables covary in time or space (Thomson & Emery, 2014). The Pearson correlation coefficient ranges from -1 to 1, where 1 implies perfect correlation, -1 implies perfect correlation but out of phase, and values close to zero equals low correlation. The model output contains values per hour, while the observed data is sampled every 20 minutes. I extracted every third data point from the observational data and calculated the correlation coefficient

between the datasets using the coinciding values per hour.

Figure 4.3 presents the Pearson correlation coefficient between each grid point represented by the dots and the stations. The gray squares enclose the selected grid points (Table 4.2). The axes represent the model coordinates for the u-component of the current velocity. The upper panels display the correlation at 282 m depth, and the lower panels display the correlation at 153 m depth. The figure displays the correlation between station N and the subarea (a,b), station M and the subarea (c,d), and station S and the subarea (e,f).

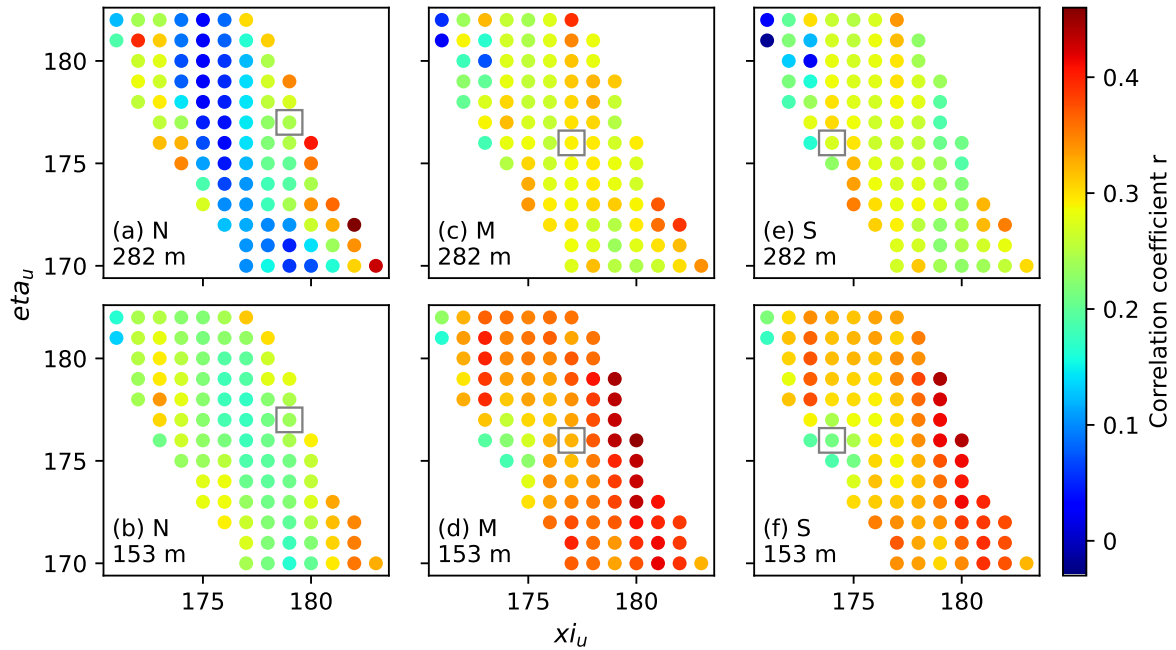


Figure 4.3: Correlation between the observed along fjord current speed and the simulated along fjord current speed in a subarea of the model domain. The upper panels display the correlation at 282 m depth (a,c,e) and the lower panels show the correlation at 153 m depth (b,d,f). The color of the dots represents the level of correlation. The axes are the model coordinates for the u-component of the velocity. The correlation is calculated using coinciding values per hour between the observations and the modeled in the period of current measurements from February to May 2022.

The correlation between station N and the subarea shows an interesting pattern along the middle of the fjord (Figure 4.3a,b). The pattern is most pronounced at 282 m depth, where the correlation coefficients are close to zero. The coefficients have higher values in the lower right of the figure (4.3a), which is on the northern side of the fjord to the east of station N (Figure 3.1c). At 153 m depth, there are also low values in the middle of the fjord (Figure 4.3b). The correlation with stations M and S shows higher values, especially at 153 m depth (Figure 4.3d,f), with the highest values on the northern side of the fjord (to the right in the figures). Around station S at 153 m depth, the correlation coefficients are lower than elsewhere in the subarea. However, the maximum correlation coefficient is 0.46, which implies a generally low correlation between the observed and modeled along fjord currents.

I chose to investigate the modeled and observed current field at 282 m depth and 153 m depth. The reason for comparing the current fields at 282 m depth is that currents along the bottom

of fjords are not well investigated, neither by observations nor the present model. Norkyst800 and Norfjords160 are more commonly validated at shallower depths regarding the study of salmon lice dispersion between fish farms (Dalsøren et al., 2020). The area where the stations are located is slightly shallower than the deeper basins on both sides (Figure 3.1c). Potential dense bottom currents propagating into the fjord will likely be detected here unless the vertical extent of the current is sufficiently small to flow beneath the instruments. 282 m depth is the second deepest level in the observations, which matched well with the depth of the second deepest layer in the model.

There are two main reasons for studying the current field at 153 depth. Firstly, I want to get an impression of the dynamics higher up in the water column in Førdefjorden, and if there are any significant differences in the model performance at this depth and along the bottom. Secondly, I release particles at 150 m depth in scenario S3, which is a realistic future scenario according to the impact assessment by Nepstad & Rye (2014). It is therefore essential to validate the model at this depth to further examine the particle dispersion in scenario S3.

### 4.1.3 Current field validation

This section contains a comparison of the observed and simulated current fields at stations and corresponding grid points at 282 m and 153 m depth. Table 4.3 contains the calculated extreme values, means, and standard deviations of the raw data from stations and grid points at 282 m and 153 m depth, including the root mean square error (RMSE). The RMSE is a measure of the mean spread of the modeled data error compared to the observed data at every corresponding data value. I calculated the RMSE between the observed and modeled datasets using the coinciding data points every hour (Table 4.3). The observed datasets at 282 m depth contain missing values of 0.9% at stations N and S, and 0.7% at station M. At 153 m depth, the amount of missing values are 0.5% at station N, 0.9% at station M, and 2.7% at station S. The missing values are linearly interpolated to avoid extracting the missing values. These observed datasets with an hourly time resolution are also used to convolve the data presented in Figures 4.5(a-c) and 4.6(a-c).

The current roses in Figure 4.4 present the raw data of simulated and observed current velocity at station N (a,b), station M (c,d), and station S (e,f) from February to May 2022 at 282 m depth. Note that the observed data contains three times more data points than the modeled data. The bins show the direction in which the currents are propagating towards, in addition to the occurrences of the different directions given in percent. The observed and simulated current velocities show a similar pattern at this depth, and the prevailing current directions are aligned with the fjord axis. At station N, water masses propagate more frequently out of the fjord than into the fjord (Figure 4.4a,b), which is additionally confirmed by the negative mean values (Table 4.3). However, the observed and simulated minimum and maximum current speeds indicate stronger currents going into the fjord than currents going out of the fjord.

At stations M and S, the currents are mainly directed into the fjord (Figure 4.4c-f), and the mean values are positive (Table 4.3). The minimum and maximum observed current speeds at station S are higher than the simulated minimum and maximum current speeds. However, the model overestimates the speed and frequency of currents going into the fjord at station M (Figure 4.4c) and has a maximum value of  $0.22 \text{ m s}^{-1}$  compared to the observed maximum

Table 4.3: The minimum, maximum, mean, standard deviation, and the root mean square error (RMSE) of the simulated and observed along fjord current speed at 282 m and 153 m depth from February to May 2022.

| <b>Stations at<br/>282 m depth</b> | Min<br>[m s <sup>-1</sup> ] | Max<br>[m s <sup>-1</sup> ] | Mean<br>[m s <sup>-1</sup> ] | Std<br>[m s <sup>-1</sup> ] | RMSE [m s <sup>-1</sup> ] |
|------------------------------------|-----------------------------|-----------------------------|------------------------------|-----------------------------|---------------------------|
| N MOD                              | -0.11                       | 0.16                        | -0.00                        | 0.03                        | 0.04                      |
| N OBS                              | -0.12                       | 0.14                        | -0.00                        | 0.03                        |                           |
| M MOD                              | -0.11                       | 0.22                        | 0.03                         | 0.05                        | 0.06                      |
| M OBS                              | -0.17                       | 0.16                        | 0.01                         | 0.03                        |                           |
| S MOD                              | -0.07                       | 0.13                        | 0.01                         | 0.03                        | 0.04                      |
| S OBS                              | -0.10                       | 0.15                        | 0.01                         | 0.03                        |                           |
| <b>Stations at<br/>153 m depth</b> |                             |                             |                              |                             |                           |
| N MOD                              | -0.09                       | 0.11                        | 0.00                         | 0.03                        | 0.04                      |
| N OBS                              | -0.19                       | 0.14                        | -0.00                        | 0.04                        |                           |
| M MOD                              | -0.09                       | 0.16                        | -0.01                        | 0.04                        | 0.05                      |
| M OBS                              | -0.16                       | 0.15                        | -0.00                        | 0.04                        |                           |
| S MOD                              | -0.09                       | 0.08                        | -0.01                        | 0.03                        | 0.04                      |
| S OBS                              | -0.17                       | 0.16                        | -0.01                        | 0.04                        |                           |

value of  $0.16 \text{ m s}^{-1}$  (Table 4.3). The model additionally underestimates the outgoing currents at station M compared to the observations (Figure 4.4c,d). The minimum simulated current speed is  $-0.11 \text{ m s}^{-1}$  and the minimum observed current speed is  $-0.17 \text{ m s}^{-1}$ .

Figures 4.5 and 4.6 show the simulated and observed along fjord current speed at the three stations at 282 m and 153 m depth, respectively. The green colors represent the modeled current speed, while the purple colors show the observed current speed. The data presented as the bold lines in the time series in Figures 4.5(a-c) and 4.6(a-c) are convolved with a 48 hour low-pass filter. The thin lines represent the raw data. I normalized the data displayed in the histograms (Figures 4.5d-f, 4.6d-f), such that the occurrences are comparable despite the difference in time resolution.

The observed and modeled along fjord currents at station N (a,d) and S (c,f) at 282 m depth correspond well (Figure 4.5). The model has more occurrences of current speeds close to zero at stations (Figure 4.5d,f). There is an event of stronger currents in mid-April visible in both the observations and the simulated current speeds. At station N, the model simulated an inflow of water during this event, while the observations show an outflow (Figure 4.5a). The model overestimates the inflow in April at station M (Figure 4.5b), while it underestimates the inflow of water at station S compared to the observations (Figure 4.5c). There is a general overestimation of water going into the fjord at Station M, as also evident in the current rose (Figure 4.4c). The histogram also shows that the distribution of modeled currents is shifted towards higher positive values compared to the observations (Figure 4.5e).

There are strong currents going into the fjord in February at 282 m depth at station M reaching  $0.2 \text{ m s}^{-1}$  (Figure 4.5b), which is also evident at stations N and S, but weaker. There are in

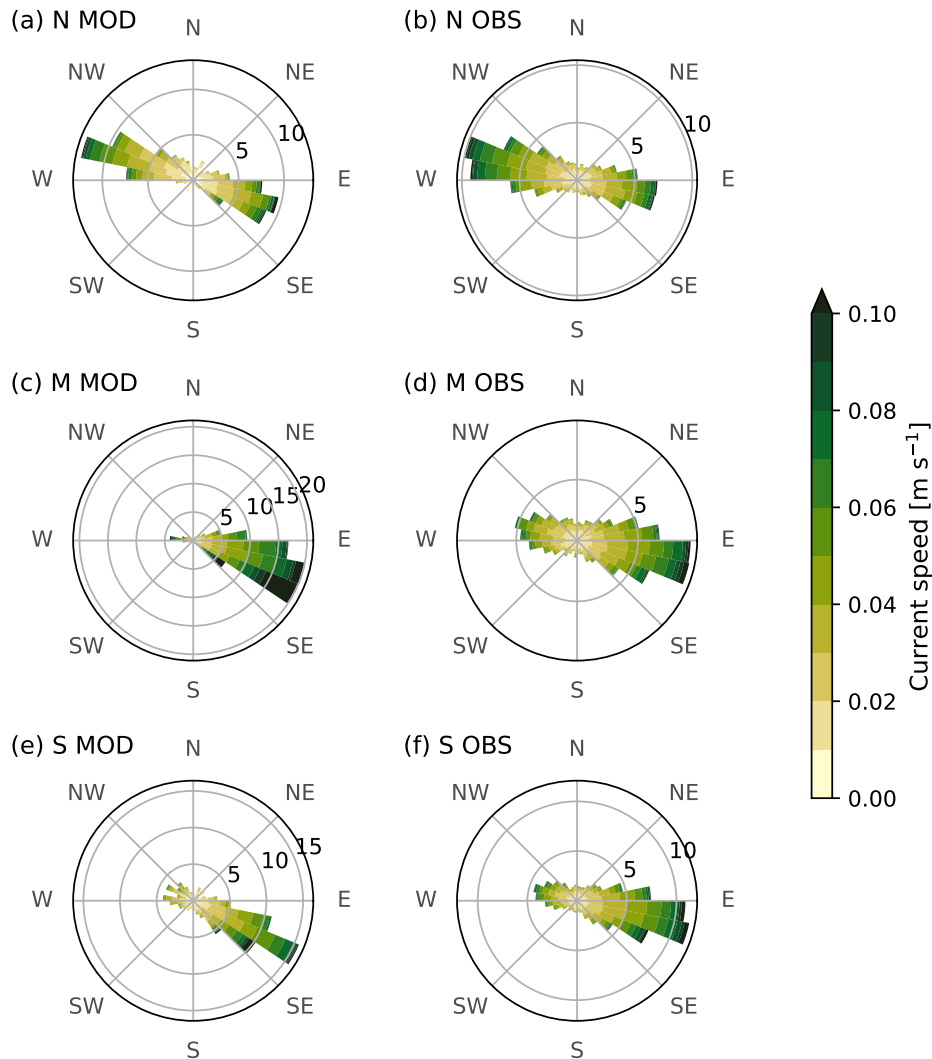


Figure 4.4: Modeled and observed current velocity at 282 m depth for station N (a,b), station M (c,d), and station S (e,f) from February to May 2022. The colorbar represents the current speed and the axes show the percentage of the occurrence of each speed bin in the given direction.

addition relatively strong currents observed at 153 m depth in February at all stations (Figure 4.6a-c). At the beginning of March, the model simulates strong currents directed into the fjord, while the observations vary between currents directed into and out of the fjord (Figure 4.6b). During the end of May at station N, the model simulates a constant inflow of water, while the observations show an outflow of water during the same period (Figure 4.6a). The event of strong currents along the bottom in April (Figure 4.5a-c) is not as evident at 153 m depth. There is a minor outflow of water in the observations at 153 m depth at station S before mid-April (Figure 4.6c), and a minor inflow in the observations at station N (Figure 4.6a). The model simulates currents in the opposite directions at this time for both stations.

The histograms in Figure 4.6(d-f) display the frequency of the different current speeds in the model and the observations at 153 m depth. The histograms show a relatively good agreement between the observed and modeled current speeds at each station. The range of simulated current speeds lies within the range of the observed current speeds at stations N and S (Fig-

ure 4.6c,f), but the model simulates more currents close to zero compared to the observations at these stations. The distribution of simulated current speed at station M is shifted towards higher positive values compared to the observations (Figure 4.6e), which was also evident at 282 m depth (Figure 4.5e). There are also more frequently weak outgoing currents in the model than in the observations at station M.

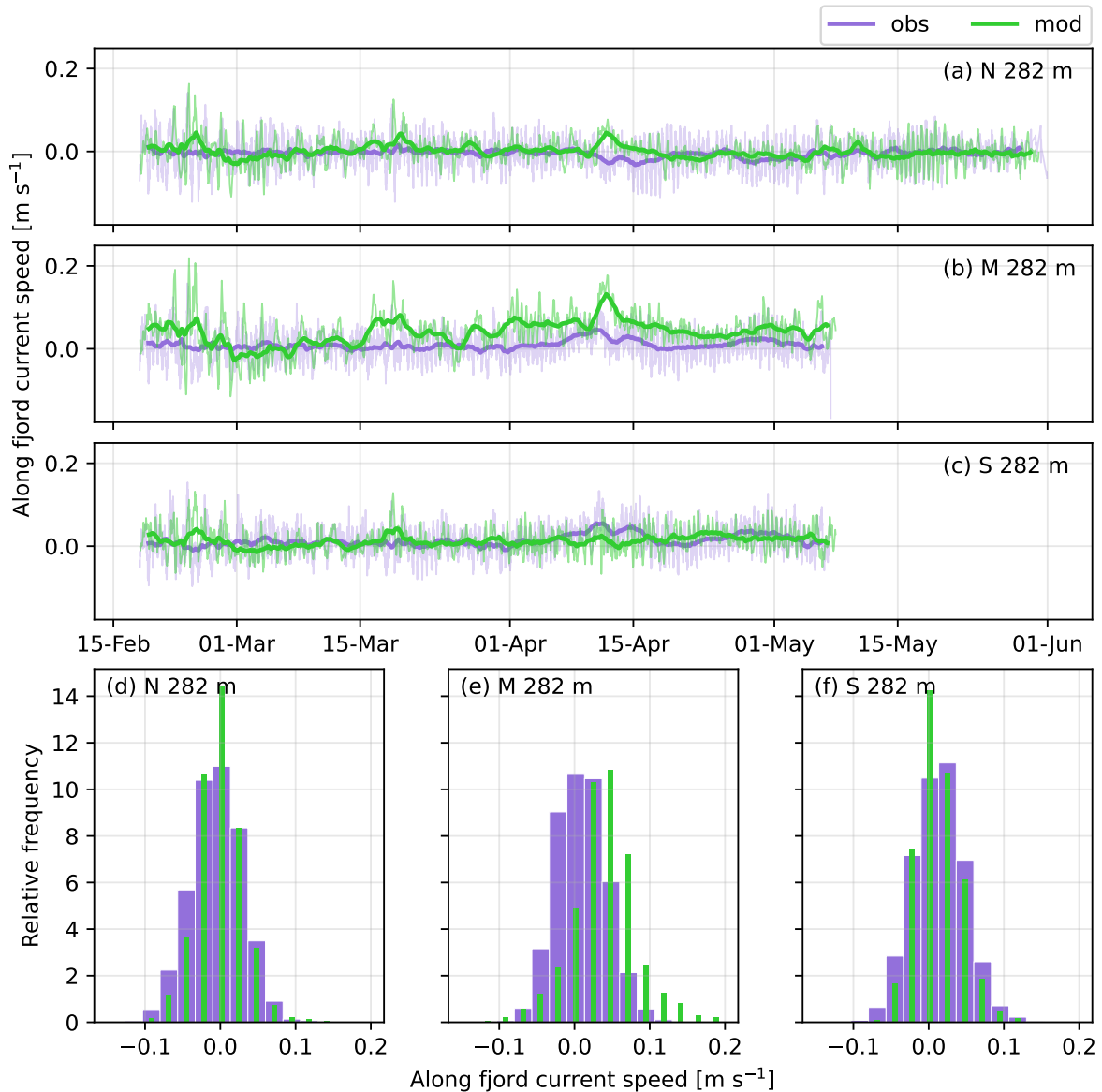


Figure 4.5: Modeled and observed along fjord current speed at 282 m depth at the northern station N (a,d), the mid station M (b,e), and the southern station S (c,f) from February to May 2022. The data presented as the bold lines in the timeseries is convolved with a 48 hour low pass filter. The data shown in the histograms is normalized, since the observed data includes three times more data points than the modeled data.

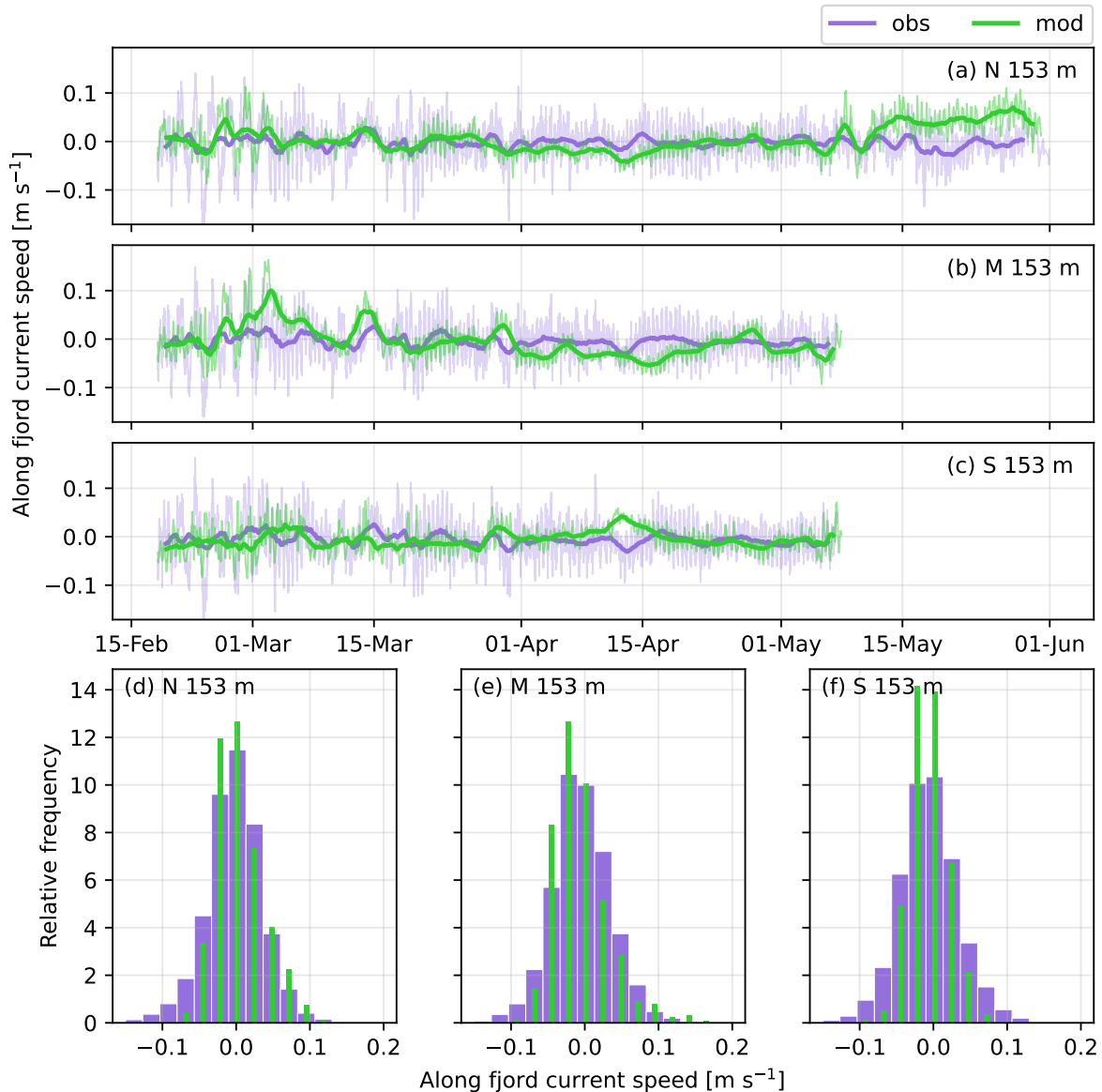


Figure 4.6: Modeled and observed along fjord current speed at 153 m depth at the northern station N (a,d), the mid-fjord station M (b,e), and the southern station S (c,f) from February to May 2022. The data presented as the bold lines in the time series are convolved with a 48-hour low pass filter. The data shown in the histograms is normalized since the observed data includes three times more data points than the modeled data.

I include the simulated current speed from the total simulation period together with observations to get an impression of the model performance during the whole year, and whether the simulated current speeds seem realistic or not. Figure 4.7 shows the along fjord current speed for the total simulation period at station S at 282 m depth together with the observed current speed. A figure displaying all stations can be found in the Appendix (Figure C.1). The data is filtered with a weekly running mean filter shown as the bold line, with the raw data as the thinner line. The currents are mainly directed into the fjord at station S (Figure 4.7), which is also evident in the current roses (Figure 4.4e,f). There are about seven events with current speeds greater than  $0.1 \text{ m s}^{-1}$ , which are relatively strong current speeds along the bottom of

the fjord. However, the magnitude of the peaks during the year of simulations is similar to the magnitude of the peak in the observations during April (Figure 4.4). The strongest inflows are during late autumn and winter.

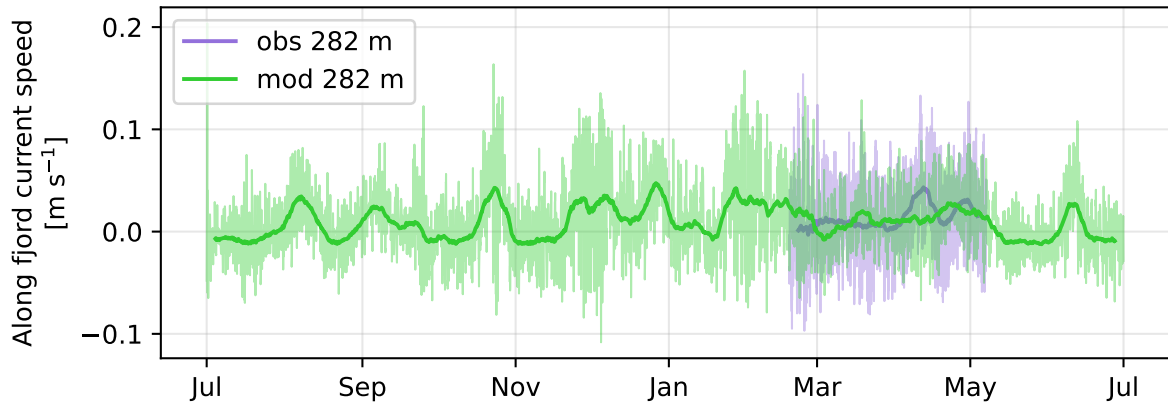


Figure 4.7: Simulated along fjord current speed from the whole simulation period and the observed along fjord current speed from February to May 2022 at station S at 282 m depth. The bold lines represent filtered data with a weekly running mean filter, and the thin lines present the raw data. Positive current speed is directed into the fjord and negative current speed is directed out of the fjord.

To investigate the model performance further, I compare the modeled and observed along fjord current speeds at 282 m and 153 m depth in terms of quantile-quantile (qq) plots (Figure 4.8). The qq-plots visualize the model performance compared to the observations. The modeled current velocity is on the y-axis and the observed current velocity is on the x-axis. Note that the speed range on the axes differs between the plots. If the dots are aligned with the red line, the observed and modeled data are alike. At positive values with dots above the line imply that the model overestimates the speed, while dots beneath the line imply that the model underestimates the speed. Negative values with dots above the line indicate that the model underestimates, while dots beneath the line indicate that the model overestimates the current speeds.

The upper panels display the comparison between simulated and observed along fjord current speed at 282 m depth (Figure 4.8a-c). The observed and modeled current speed corresponds well at station N, with an underestimation at higher positive values (Figure 4.8a). The comparison at station M shows a general overestimation of the current speed (Figure 4.8b), while the model underestimates the current speed at station S (Figure 4.8c). At 153 m depth, the model underestimates the current speed at all three stations and most evidently at the minimum values (Figure 4.8d-f). There is also a clear underestimation at higher positive values at station S (Figure 4.8f).

There is a general pattern of the model not resolving the higher absolute values of the current speed compared to the observations, by either over- or underestimating the current speed. The pattern is evident throughout the comparison conducted in this section.

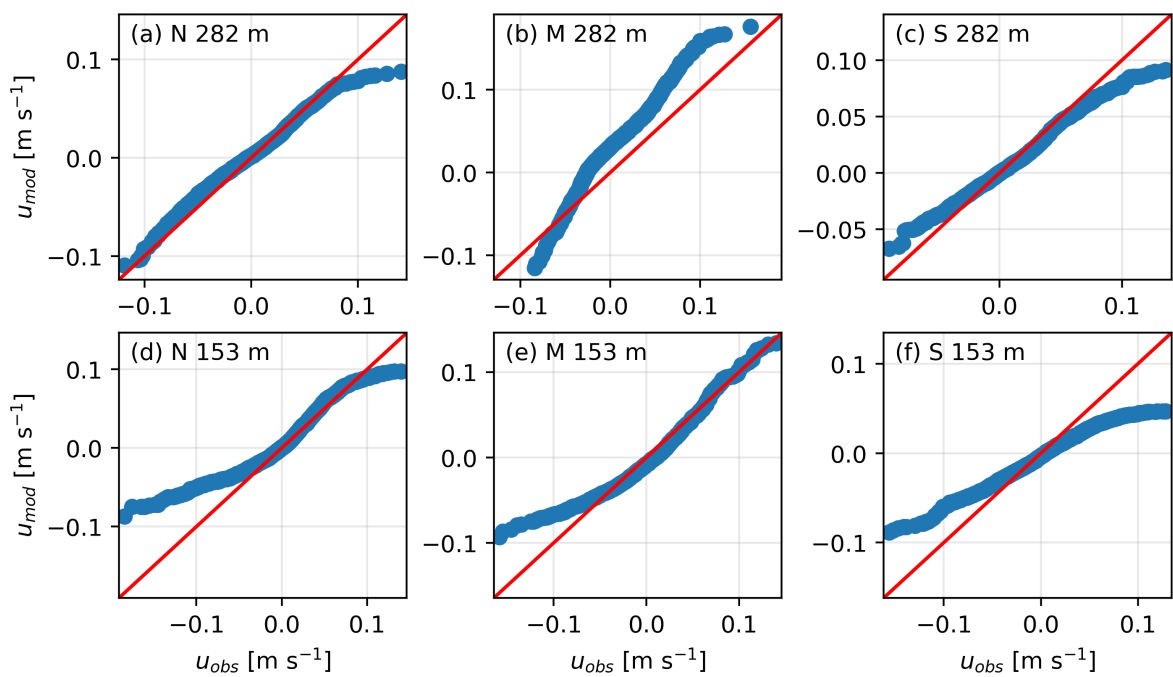


Figure 4.8: Quantile-quantile plots of observed and simulated along fjord current speed at station N (a,d), station M (b,e), and station S (c,f). Upper panels are at 282 m depth (a-c), and lower panels are at 153 m depth (d-f). Modeled data along the y-axis, and observed data along the x-axis.

## 4.2 Horizontal current field around the STD site

This section presents a comparison of the current fields around the STD site with the present and modified bathymetry. I want to examine how the modified bathymetry influences the current field in the model. I therefore compare the yearly means of the current field with present and modified bathymetry at 100 m depth (Figure 4.9a,b) and 150 m depth (Figure 4.9c,d). Since the model output is in sigma coordinates, I interpolated the current velocity data to the given z-depths using the Zslice function from the Ropyy package (Ådlandsvik, 2023). Ropyy is made for visualizing ROMS output data. The upper panels in Figure 4.9 have the present model bathymetry, while the lower panels include the modified bathymetry presented in Figure 3.1d. The arrows represent the current velocity and the colormap shows the current speed.

The current fields at 100 m depth with different bathymetries look similar except for a higher current speed in the STD area (Figure 4.9a,b). There is a cyclonic and anticyclonic motion in the STD area in both cases, where the speed is higher in the cyclonic motion in (b). Further, the mean current at 100 m depth is propagating out of the fjord from the STD area along Hegreneset (Figure 4.9a,b), which is the headland in the middle of the subplots. Both current fields along Hegreneset are diverging from the cyclonic motion at the STD site towards the southern side of the fjord, and flowing towards the northern side again at the tip of Hegreneset. The mean current speeds are increasing there in both cases, and the currents split into either going further out of the fjord or into the anticyclonic motion.

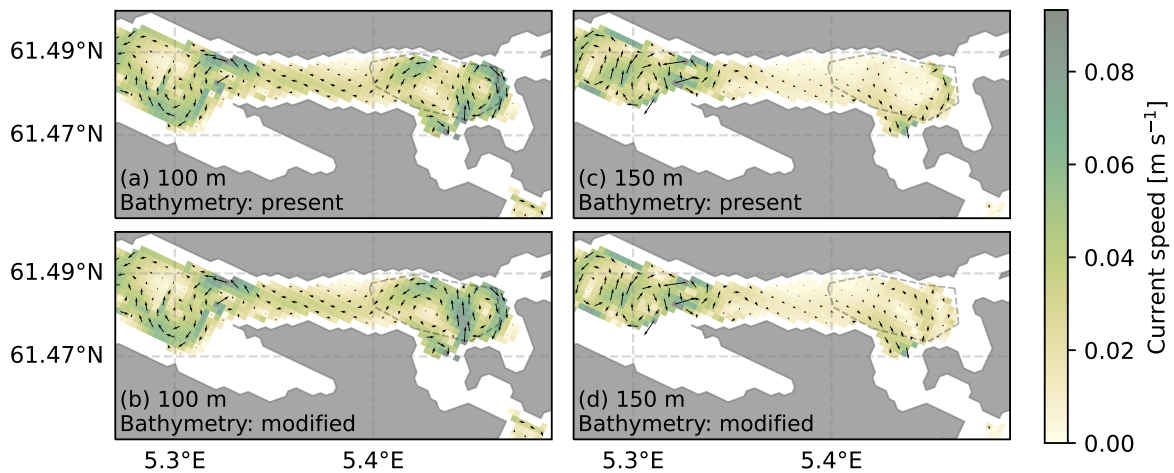


Figure 4.9: Simulated current field at and around the STD area at 100 m depth (a,b) and 150 m depth (c,d). The upper panels include the present bathymetry (a,c), while the lower panels have the modified bathymetry (b,d). The arrows show current velocity and the colormap shows the current speed. The STD site is marked by the gray dashed lines.

Figure 4.9(c,d) show the current fields from 150 m depth, which also look very similar. The mean currents outside Hegreneset have a less confined motion pattern in both cases, compared to at 100 m depth (a,b). The mean current along Hegreneset is in addition directed towards the STD site in the cases from 150 m depth (Figure 4.9c,d). There is a cyclonic current pattern in the STD area for case (d) with modified bathymetry, which is not visible in case (c) with present bathymetry. The mean current speeds are weaker at the STD site for the cases at 150 m depth. However, the maximum mean current speeds at 150 m depth are  $0.099 \text{ m s}^{-1}$  for both cases, which is slightly higher than for cases (a) and (b) of  $0.093 \text{ m s}^{-1}$  and  $0.094 \text{ m s}^{-1}$ .

### 4.3 The coastal and local wind field

In this section, I present the coastal wind outside of Fjørdefjorden and the local wind in the fjord to further examine the possible effects of wind on the fjord circulation. The coastal wind is from Ytreøyane, and the along fjord wind is from Vevring (Figure 3.1b,c). The wind roses in Figure 4.10 show the wind velocity at the given locations. Note that the direction of the bins corresponds to the direction in which the wind is going towards, i.e. the opposite of a wind rose used in meteorology. The wind roses show that the prevailing wind direction at the coast is north-south, i.e. along the coast axis, and east-west along the fjord axis. There is more spread in the wind direction at Vevring including some cross-fjord winds (Figure 4.10b), but they are not as evident as the along fjord winds. The wind at the coast is substantially stronger than the wind along the fjord (Figure 4.10).

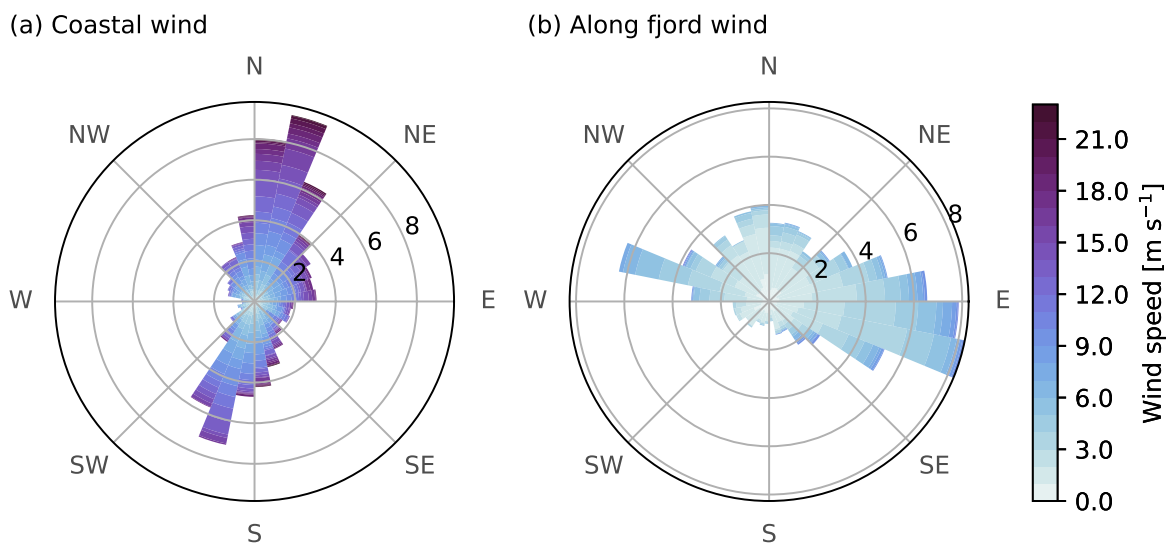


Figure 4.10: Simulated wind velocity from AROME at Ytreøyane (a) and Vevring (b) from July 2021 to June 2022. The direction of the bins corresponds to the direction of where the wind is going towards.

Figure 4.11 shows the wind speed along the coast at Ytreøyane (a) and along the fjord at Vevring (b). The solid lines in both panels present the low pass filtered data with an averaging window of a week, while the thin lines present the low pass filtered data with an averaging window of a day (Figure 4.11). The data is from July 2021 to June 2022. There are often wind episodes with absolute wind speed exceeding  $10.0 \text{ m s}^{-1}$  at Ytreøyane, and there are also frequently wind speeds reaching  $20.0 \text{ m s}^{-1}$  (Figure 4.11a). The maximum wind speed at Ytreøyane is  $23.0 \text{ m s}^{-1}$ . The duration of the strong wind events is modest and lasts typically for less than a day. The mean wind speed is  $1.7 \text{ m s}^{-1}$ , indicating that there are more southerlies than northerlies during that year. This is also visible in the wind rose (Figure 4.10a). The wind is quite strong from the end of February to the end of March (Figure 4.11a). During April, the wind shifts between northerlies in the beginning of the month, to southerlies in mid-April, and northerlies again towards the end of the month.

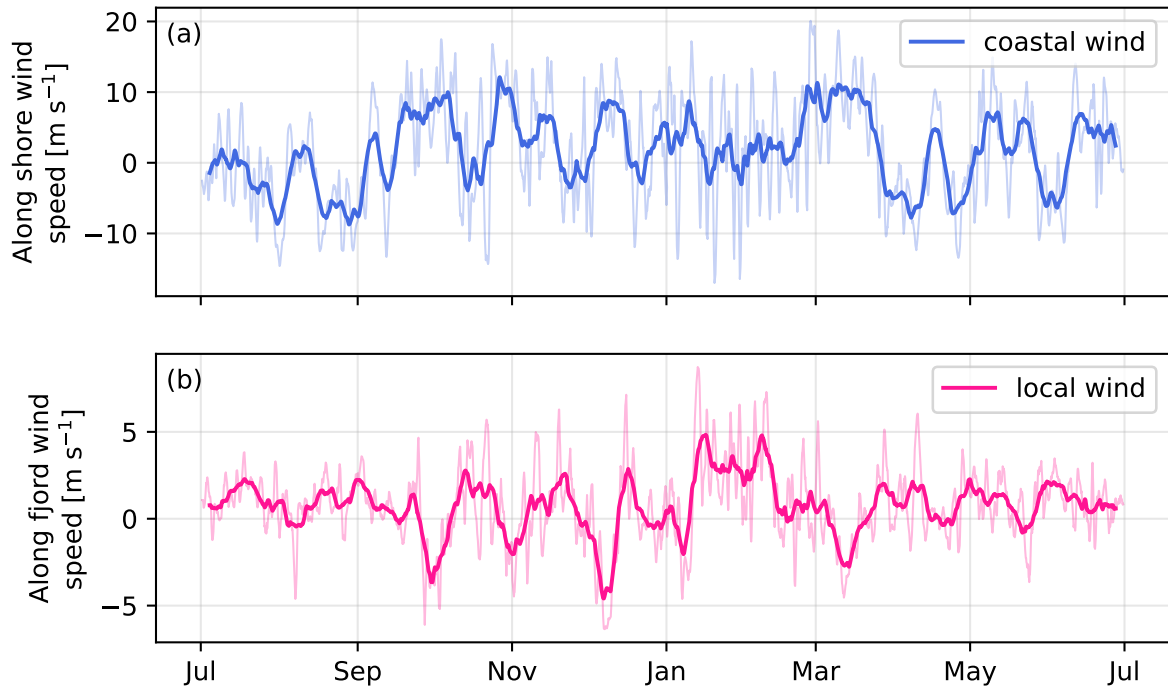


Figure 4.11: Simulated wind from AROME at Ytreøyane (a) and at Vevring (b) from the total period. The upper panel includes the  $v$ -component of the wind speed only, while the lower panel includes the  $u$ -component of the wind speed. The data presented as the bold lines in both panels are filtered with a low pass filter with an averaging window of a week, while the thin lines are filtered with a low pass filter with an averaging window of a day.

At Vevring, the wind conditions are calmer with a maximum speed of  $10.0 \text{ m s}^{-1}$  (Figure 4.11b). The mean wind speed throughout the year is  $0.7 \text{ m s}^{-1}$ , which indicates more frequent westerly winds than easterly, i.e. winds propagating into Førdefjorden. This can also be seen in the wind rose plot (Figure 4.10b).

## 4.4 Particle dispersion

This section includes the results from the particle dispersion runs in terms of calculated sedimentation and concentration. I calculated the sedimentation of settled particles for all scenarios (Table 3.1), while I focused on the future scenarios S3 and S4 for the concentration calculations. I calculated the concentration of pelagic particles, which refers to particles in the water masses. I also look at particle dispersion during an event of stronger currents propagating into the fjord.

### 4.4.1 Sedimentation of particles

I calculated the annual sedimentation of the settled particles from all four scenarios. Figure 4.12 shows the calculated sedimentation with 1% fine fraction, which corresponds to the amount of released particles. Figure 4.13 displays the sedimentation of the particles with a mass corresponding to a fine fraction of 5% of the total mine tailing. The blue color shows sedimentation  $\geq 3$  mm, corresponding to sedimentation exceeding the regulation limits (Table 1.1).

The sedimentation of 1% fine fraction shows a pattern in all scenarios of particles settling along the basin that the STD area extends into (Figure 4.12). The basin is visible in Figure 4.16. Scenario S1 has a release depth at 280 m and represents the start of the mine tailing disposal. There is sedimentation of particles  $\geq 3.0$  mm yr<sup>-1</sup> close to the border of the STD area (Figure 4.12a). The sedimentation outside the STD area exceeds the limit of  $>3.0$  mm yr<sup>-1</sup> already in S2, which has a release depth of 250 m (Figure 4.12b). The sedimentation of particles is less confined in scenarios S3 and S4 (Figure 4.12c,d), with release depths at 150 m and 100 m depth, respectively. There is a higher rate of sedimentation outside the STD area for these two scenarios, both west and south of the STD site. In S4, there is a pronounced increase in sedimentation at Ålasundet towards the inner part of the fjord.

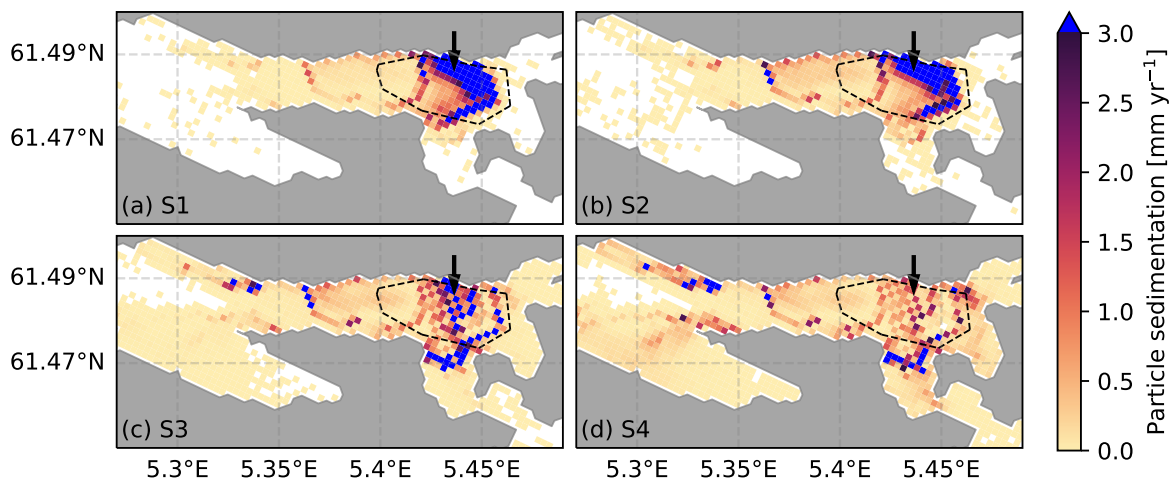


Figure 4.12: Calculated annual sedimentation of particles for scenarios S1 (a), S2 (b), S3 (c), and S4 (d). The scenarios in the upper panels (a,b) have present bathymetry, while the scenarios in the lower panels (c,d) have modified bathymetry. Blue color indicates sedimentation  $\geq 3$  mm. The black dashed line illustrates the STD area and the arrow shows the release point of particles.

The results from setting the fine fraction to 5% show sedimentation  $\geq 3$  mm outside the STD area in all scenarios (Figure 4.13). There is a pronounced amount of particles settling in the basin to the west of the STD site in all scenarios, not only along the sides of the basin as for the sedimentation of 1% fine fraction. The rate of sedimentation of particles inside the STD area decreases for each scenario, with a corresponding increase of sedimentation further into the fjord and towards the outer part of the fjord (Figure 4.13b-d). In scenario S3 and S4, there is an accumulation of settled particles south of the STD site, at the tip of Hegreneset, and at the northern side of the fjord from the tip of Hegreneset (Figure 4.13c,d). In scenario S4, there is a distinct increase in particle sedimentation southwest of the tip of Hegreneset, and at Ålasundet (Figure 4.13d).

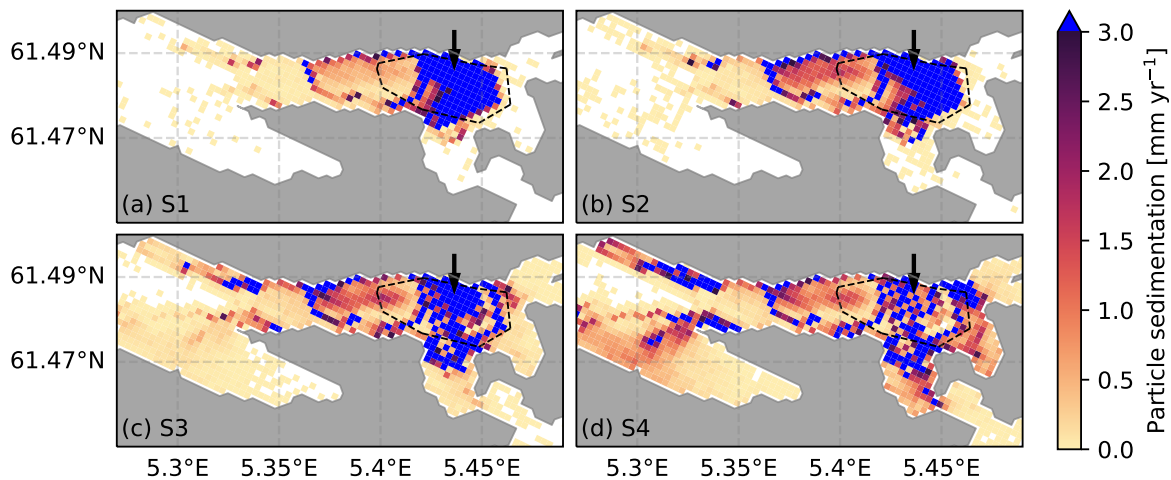


Figure 4.13: Calculated annual sedimentation of particles for scenarios S1 (a), S2 (b), S3 (c), and S4 (d), where the fine fraction is set to 5% of the total mine tailing. The scenarios in the upper panels (a,b) have present bathymetry, while the scenarios in the lower panels (c,d) have modified bathymetry. Blue color indicates sedimentation  $\geq 3$  mm. The black dashed line illustrates the STD area and the arrow shows the release point of particles.

#### 4.4.2 Concentration of pelagic particles for scenarios S3 and S4

I consider scenarios S3 and S4 for the concentration calculations, with respective release depths at 150 m and 100 m depth. I will first present the annual maximum concentration of pelagic particles at depths  $\geq 40$  m above the release depths (Figures 4.14 and 4.15). Secondly, I will present particle concentration with time at four selected grid points (Figures 4.17 and 4.18).

Figures 4.14 and 4.15 show the annual maximum concentration of particles calculated for each grid cell with a vertical bin size of 10 m. The figures include six vertical bins each, and I only look at depths  $\geq 40$  m above the release depth. The particle concentration should not exceed  $2.0 \text{ mg l}^{-1}$  at depths  $\geq 40$  m above the release depth of particles everywhere in the fjord. Outside the STD site, particle concentrations should not exceed  $3.0 \text{ mg l}^{-1}$  below the release depth. I calculated the daily concentrations from July 2021 to June 2022 in each grid cell in the given depth intervals and then calculated the maximum value from the whole period. The maximum concentration of each grid cell is displayed in Figures 4.14 and 4.15.

For scenario S3, the depth bins I consider range from 50 m to 110 m depth (Figure 4.14). There are maximum particle concentrations  $\geq 2.0 \text{ mg l}^{-1}$  at all depth intervals shown in Figure 4.14. The particles appear to drift along the northern side of the fjord at all depths, directed out of the fjord from the STD area. There is an increase in occurrences of annual maximum concentration  $\geq 2.0 \text{ mg l}^{-1}$  with increasing depth (Figures 4.14a-e).

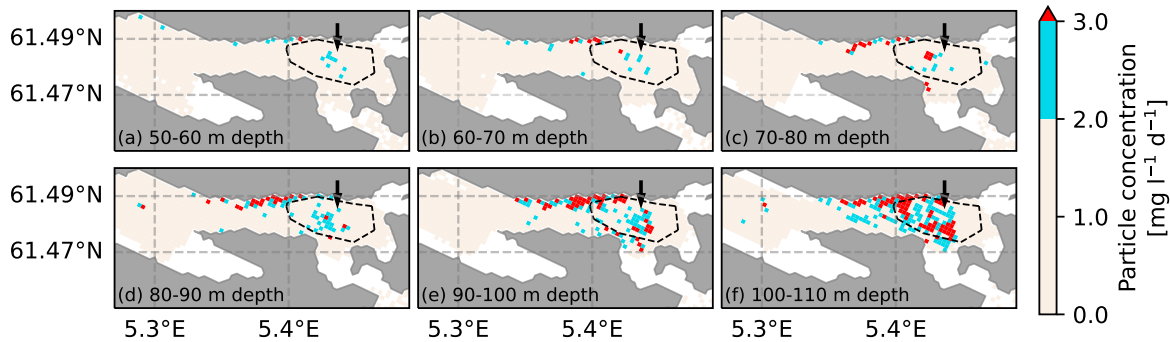


Figure 4.14: Annual maximum concentration for scenario S3 calculated for each grid cell divided into vertical bins from 50 m to 110 m depth (a-e). The release depth in scenario S3 is at 150 m. Blue color indicates concentration  $\geq 2.0 \text{ mg l}^{-1}$ , while red color indicates concentration  $\geq 3.0 \text{ mg l}^{-1}$ . The black dashed line illustrates the STD area, and the arrow shows the release point.

Figure 4.15 shows the annual maximum concentrations for scenario S4. The depth intervals range from 0 m to 60 m depth. There are more occurrences of maximum concentration  $\geq 3.0 \text{ mg l}^{-1}$  at all depths shown in scenario S4 (Figure 4.15), compared to scenario S3 (Figure 4.14). The particles seem to be advected out of the fjord along the northern side in scenario S4, as also visible in scenario S3. As in scenario S3, there is also an increase in the annual maximum concentration  $\geq 2.0 \text{ mg l}^{-1}$  with increasing depth in scenario S4 (Figure 4.15).

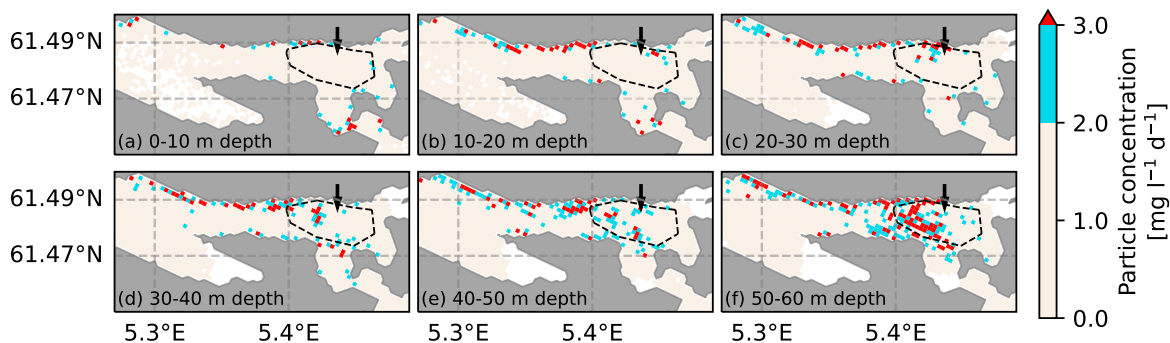


Figure 4.15: Annual maximum concentration for scenario S4 calculated for each grid cell divided into vertical bins from 0 m to 60 m depth (a-e). The release depth in scenario S4 is at 100 m. Blue color indicates concentration  $\geq 2.0 \text{ mg l}^{-1}$ , while red indicates concentration  $\geq 3.0 \text{ mg l}^{-1}$ . The black dashed line illustrates the STD area, and the arrow shows the release point.

In addition to the annual maximum concentration of pelagic particles, I also investigate the temporal distribution of the particles at four grid points for scenarios S3 and S4 from July 2021 to June 2022. I chose the four grid points based on the maximum concentration plots

(Figures 4.14 and 4.15). Figure 4.16 displays the grid points, where grid points P1 and P2 are inside the STD area, and P3 and P4 are outside the STD area. The bottom depth at grid point P1 is 246 m, while grid points P2 and P3 are in the deeper basin at 334 m depth. Grid point P4 is close to the current measurement stations, and the bottom depth is 295 m (Figure 4.16). The gray dashed line in Figures 4.17 and 4.18 shows the depth 40 m above the release depth of the particles.

Figure 4.17 shows the particle concentrations with time from grid points P1 (a,b) and P2 (c,d) inside the STD area. Concentrations should not exceed  $2.0 \text{ mg l}^{-1}$  above the gray dashed line, in accordance with the regulations (Table 1.1). The upper panels present scenario S3, and the lower panels present scenario S4. Concentrations of  $2.0 \text{ mg l}^{-1}$  and  $3.0 \text{ mg l}^{-1}$  are very close to the line throughout the year for both grid points and both scenarios, but more frequently at grid point P2 (Figure 4.17c,d). There are in addition events of particle concentration  $\geq 3.0 \text{ mg l}^{-1}$  exceeding the gray dashed line at both grid points and both scenarios. The concentrations are lower at grid point P1, especially for scenario S4 (Figure 4.17b).

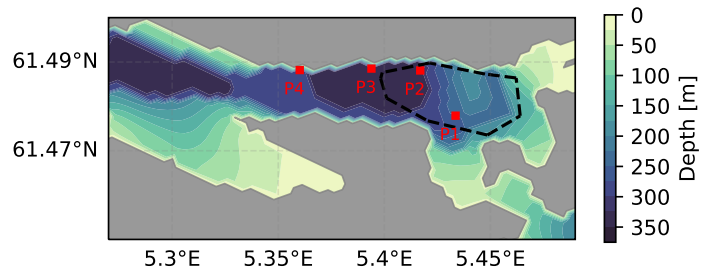


Figure 4.16: Map of the STD site and surrounding area in the model domain of Førdefjorden with grid points I chose to examine.

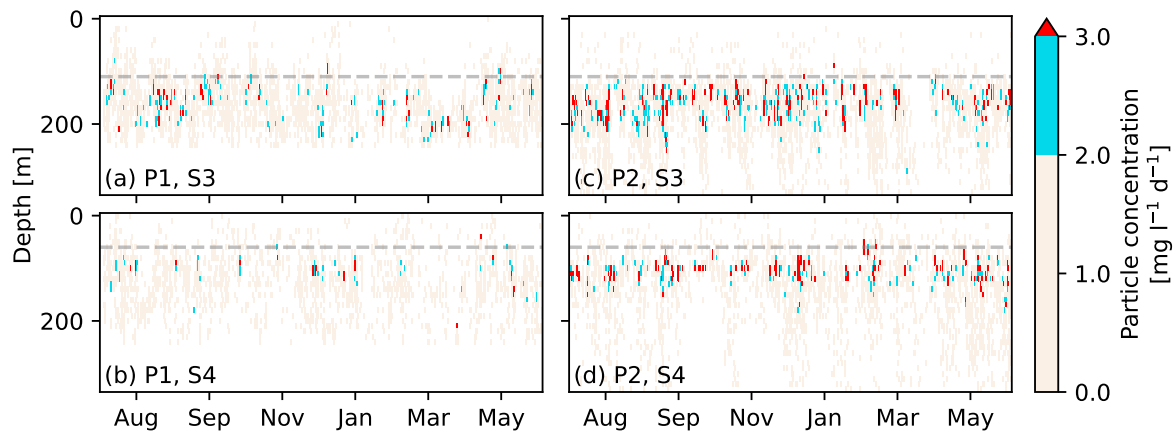


Figure 4.17: Calculated concentration of pelagic particles per day at grid points P1 (a,b) and P2 (c,d) from July 2021 to June 2022. The upper panels show the concentration from scenario S3 (a,c), and the lower panels display the concentration calculated from S4 (b,d). The blue color represents concentration  $\geq 2.0 \text{ mg l}^{-1}$ , while the red color represents concentration  $\geq 3.0 \text{ mg l}^{-1}$ . The grey dashed line marks the depth 40 m above the release depth of particles.

Figure 4.18 presents particle concentrations with time from grid points outside the disposal area. The upper panels show scenario S3 at both grid points (Figure 4.18a,c), and there seems to be more higher concentration of particles in this scenario than in scenario S4 displayed in the lower panels (Figure 4.18b,d). In accordance with the regulations (Table 1.1), concen-

trations should not exceed  $2.0 \text{ mg l}^{-1}$  above the gray dashed line, and  $3.0 \text{ mg l}^{-1}$  in the water column below the release depth outside the STD site. Thus, there should be no concentrations of  $3.0 \text{ mg l}^{-1}$  (red colors) at grid points P3 and P4, and no concentration  $\geq 2.0 \text{ mg l}^{-1}$  above the gray dashed line (Figure 4.18). However, too high concentrations appear frequently at these grid points outside the STD site.

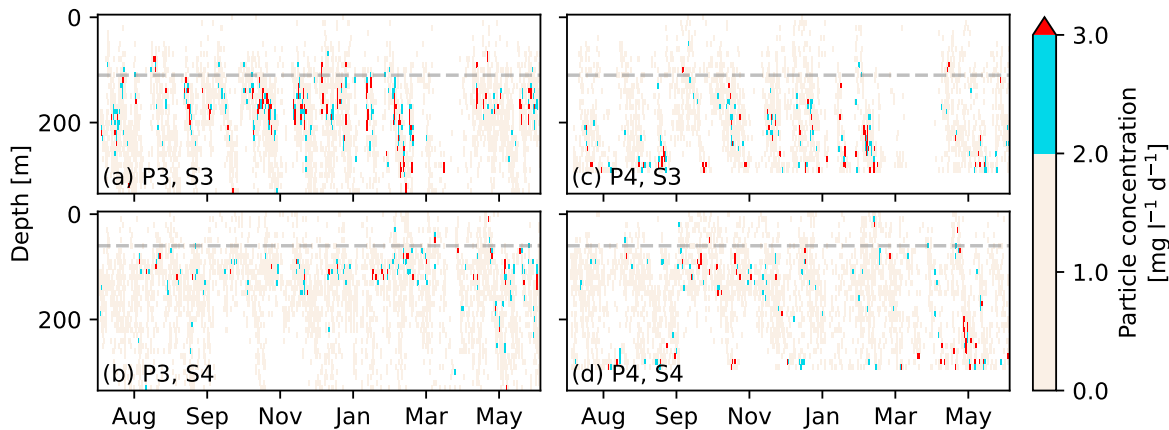


Figure 4.18: Calculated concentration of pelagic particles per day at grid points P3 (a,b) and P4 (c,d) from July 2021 to June 2022. The upper panels show concentrations from scenario S3 (a,c), and the lower panels present the concentration calculated from scenario S4 (b,d). The blue color shows concentration  $\geq 2.0 \text{ mg l}^{-1}$ , while the red color shows concentration  $\geq 3.0 \text{ mg l}^{-1}$ . The grey dashed line marks the depth 40 m above the release depth of particles.

#### 4.4.3 Convergence of pelagic particles outside the disposal area

Throughout the simulation period from July 2021 to June 2022, there are occasions of convergence of particle concentration outside the disposal area at grid points P3 and P4. I will investigate an event of higher particle concentration from the 22nd of February 2022 to the 20th of March 2022 in scenario S3 at grid point P4 (Figure 4.18c) displayed in Figure 4.19. The figure shows the particle concentration per day (a) and the along fjord current speed per hour (b), both at grid point P4. The current speed displayed in the figure ranges from  $-0.15$  to  $0.15 \text{ ms}^{-1}$ . Current speeds outside this range are colored white. Positive current speeds (red color) represent currents directed into the fjord, while negative current speeds (blue color) represent currents directed out of the fjord.

There are particles distributed in the whole water column from the 22nd of February to the 4th of March (Figure 4.19a). During the next 10 days the particle concentration is higher, and the distribution of particles is more confined at depths below 150 m. The current field fluctuates between inflowing and outflowing currents during the whole period (Figure 4.19b). The currents are stronger between the 22nd of February and the 4th of March in the whole water column and weaker beneath the surface layer after this period.

From 4th to 8th of March there are concentrations exceeding  $2.0 \text{ mg l}^{-1}$  at 250 m depth. To investigate this further, I extracted the particle concentration and the along fjord current speed at this depth presented in Figure 4.20(a). The orange lines are particle concentration, and the

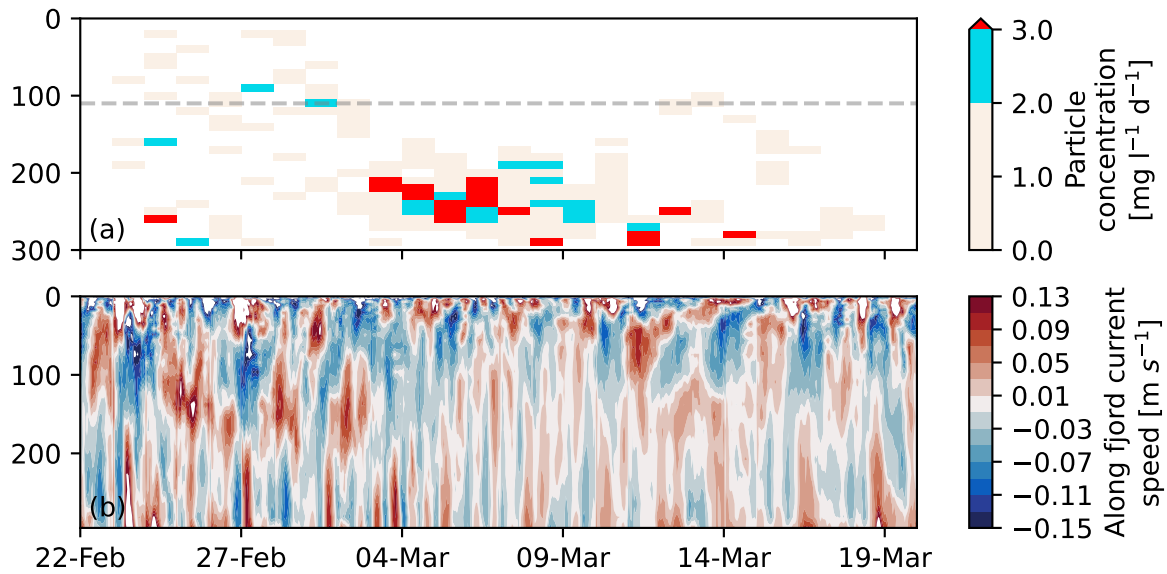


Figure 4.19: Simulated particle concentration per day from scenario S3 (a) and the along fjord current speed per hour (b) at grid point P4 from the 22nd of February to the 20th of March 2022. The blue color in (a) represents concentration  $\geq 2.0 \text{ mg l}^{-1}$ , while the red color represents concentration  $\geq 3.0 \text{ mg l}^{-1}$ . The grey dashed line marks the depth 40 m above the release depth of particles. The current speed range is set to  $-0.15$  to  $0.15 \text{ m s}^{-1}$ , and current speeds outside the range are colored white. Positive current speed is currents directed into the fjord, while negative current speed is currents directed out of the fjord.

green line is the current speed. The period is equal to the period in Figure 4.19. The along shore coastal wind speed from the same period is displayed in Figure 4.20(b). The temporal resolution of the wind data is three hours.

The fluctuation in the current field shown in Figure 4.19(b) is also evident in the current field at 260 m depth (Figure 4.20a). Between the 22th of February and the 4th of March, the current speed exceeds  $0.1 \text{ m s}^{-1}$  three times, and  $-0.1 \text{ m s}^{-1}$  once. The current speeds are weaker after the 4th of March (Figure 4.19b). The particle concentration, however, increases after the 4th of March to  $18.0 \text{ mg l}^{-1}$  on the 5th of March. Furthermore, the particle concentration exceeds  $3.0 \text{ mg l}^{-1}$  twice after the 5th of March before it decreases to zero again. The wind speeds are also highest between the 22nd of February and the 4th of March, and the maximum wind speed is  $16.0 \text{ m s}^{-1}$ . Positive wind speed implies southerly wind, which can potentially lead to downwelling at the coast outside the fjord.

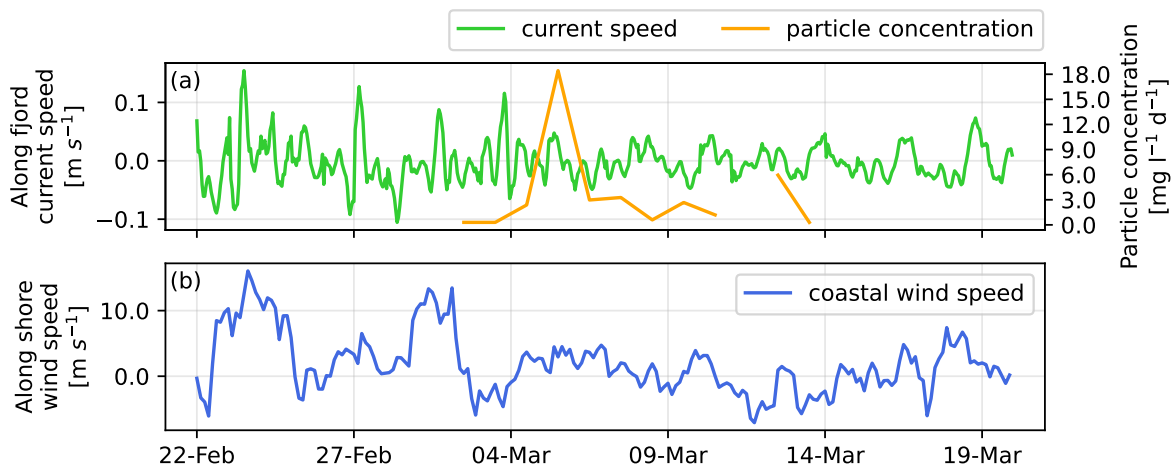


Figure 4.20: Simulated along fjord current speed and particle concentration (scenario S3) at 250 m depth (a) and simulated along shore coastal wind at Ytreøyane (b) from the 22th of February to the 20th of March 2022. The green line is the current speed (positive into the fjord) per hour, the orange lines are particle concentration per day, and the blue line is the coastal wind speed (positive towards the north) every third hour. Particle concentration equal to zero is not included, which is the reason for the discontinuous orange line.

# Chapter 5

## Discussion

This study is mainly based on model results. ROMS is a widely used ocean model. The coastal model Norkyst800 and the fjord model Norfjords160 are largely used to study the dynamics along the Norwegian coast and inside fjords, and additionally the dynamics between the coast and the fjords (Albretsen et al., 2022). The models correspond well with observations, but when investigating dispersion of for instance mine particles, it is essential to evaluate the model performance (Dalsøren et al., 2020). In this chapter, I will first discuss the model performance of Førdefjord160. I will examine possible reasons for the deviations between the model output and the observations, including limitations regarding both the model and the observations. Secondly, I will compare the particle dispersion scenarios. I will discuss potential causes for the variations between and within the scenarios.

### 5.1 Validation of the Førdefjord160 model

The general results from the current field validation of Førdefjord160 imply that the model simulates a realistic current field in Førdefjorden. The results from the comparison at 282 m depth show that the model overestimates the speed of the inflowing currents in the middle of the fjord, i.e. at station M (Figures 4.4 and 4.5, Table 4.3). The model underestimates the speed of the inflowing current along the northern and southern sides of the fjord, that is stations N and S. At 153 m depth, the model underestimates current speeds out of the fjord at all stations (Figures 4.6 and 4.8). There is also an underestimation of current speeds into the fjord at stations N and S. Thus, the model does not capture the higher absolute values of the current speed properly in comparison with the observations. However, the modeled current speed range and the direction of the currents generally coincide with the observed currents.

I investigated the salinity and temperature fields in the model for the whole simulation period and compared the fields with CTD stations available from the same period and location. The temperature and salinity fields in the model showed seasonal patterns, including high temperatures in the surface layer during the summer and autumn months, and lower temperatures in the surface layer during the winter months (Figure 4.1). The surface layer is relatively fresh throughout the simulation period, except in August, September, and April. The comparison between the CTD profiles and the corresponding modeled data showed a tendency for the model to be fresher and colder than the observations (Figure 4.2).

The comparison of modeled and observed hydrography in December shows that the model has

a warm and fresh bias below 100 m depth (Figure 4.2b). The model also has a warm bias below 100 m depth in October and February (Figure 4.2a,c). The deviations in the mean temperatures and salinities between the model and observations are within 1.1 °C and 2.0 PSU. How the model resolves the hydrography has also been investigated in other fjord systems such as Altafjorden (Skarðhamar et al., 2018), the Folda fjord system (Myksvoll et al., 2011; Johnsen et al., 2016), and Hardangerfjorden (Asplin et al., 2020). The stratification affects the circulation in fjords, and too weak simulated stratification at the coast can lead to weakened internal wave propagation into the fjord (Dalsøren et al., 2020). Skarðhamar et al. (2018) find that the model simulates a weaker stratification in the upper 15 m in Altafjorden in comparison with observations. In Folda, the model tends to simulate too strong stratification in the upper five meters and too weak stratification beneath (Myksvoll et al., 2011). The results from Johnsen et al. (2016) show that the model had slightly lower temperatures and higher salinity values than the observations. Asplin et al. (2020) examine the model performance of Norkyst800 in Hardangerfjorden and at various locations along the Norwegian coast. They find that the model has a fresh bias in the upper 100 m and a general warm bias, but the deviations are minor. In my results, the model has a warm bias below 100 m. However, there does not seem to be persistent bias in the model according to these studies, and the possible reasons for the deviations vary. Johnsen et al. (2016) found that tides caused large variations in simulated salinity and temperature per day. Asplin et al. (2020) discuss that possible reasons for the discrepancies between the simulated and observed current field in Hardangerfjorden are due to deviations in the coastal density field or discrepancies in the wind forcing. Dalsøren et al. (2020) present a new validation method for hydrodynamic fjord models and also find that poor model performance can be connected to deviations in the coastal stratification.

The dynamics simulated by the model can be shifted temporally and spatially compared to the actual dynamics in the fjord and can lead to poor results of RMSE and correlation coefficients (Albretsen & Asplin, 2021; Sandvik et al., 2016). The RMSE values are larger or equal to the standard deviations of the current speeds (Table 4.3). I find it hard to interpret the magnitude of the RMSE. However, similar values of the RMSE between simulated and observed currents are found in Skarðhamar et al. (2018), which implies that the high values are not specific to this work. I calculated the correlation and RMSE using every coinciding value per hour. A consistent temporal and/or spatial lag in the model can therefore be the reason for the poor correspondence shown by these estimates. There is a good agreement between the observed and modeled direction of the flow, in addition to the occurrence of the different magnitudes of the current speeds (Figures 4.4, 4.5, and 4.6). Furthermore, the correlation at stations N and S is not significantly higher than at station M with the pronounced overestimation of the current speed (Figure 4.3). Thus, this can imply that a major reason for the poor correlation and RMSE between the model and the observations is a general temporal lag in the model compared to the observations. However, the estimates of extreme values, means, and standard deviations show a good correspondence between the simulated and observed current fields.

The RMSE quantifies the error of the model compared to the observations, although the observations have limitations as well. The combination of observations and model results gives a prediction of the actual conditions in a fjord (Skogen et al., 2021). The observations are typically a compromise between temporal and spatial resolution. Current measurements often have good temporal resolution but during a limited period and at fixed locations. A CTD cast can give a good spatial representation of a fjord but in a limited period of time. The current measurements used in this project only present the current at three positions across the fjord.

The error in the representativeness of the observations is unknown and can be crucial. Variations in topography can cause the moorings to be placed at shallower depths than the deepest point in the area. Thus, there might be stronger currents in the area than the observations suggest. It can also be the case that the moorings are placed in a depression where the measured currents are stronger than in the surrounding area. Skarðhamar et al. (2018) discuss the error in the scarce observations in time and space compared to the Norkyst800 model. The modeled and measured variability cannot be expected to correspond perfectly in time and space, especially at spatial scales smaller than the horizontal resolution of the model.

The comparison of simulated and observed current speed at station M at 282 m depth showed an evident overestimation of currents directed into the fjord (Figures 4.4c, 4.5b,e, and 4.8b). A possible reason can be a discrepancy in the boundary forcing in the model. Dalsøren et al. (2020) found that the model performance of Norfjords160 was poor compared to observations when internal waves generated by pressure perturbations at the coast did not propagate far enough into the fjord. They assume that the cause can be deviations in the coastal stratification in the model connected to fluctuations in the boundary conditions. If the coastal stratification is overestimated at depth by Førdefjord160, bottom currents can appear too frequent in the fjord.

The deviations between the model and observations regarding stronger in and outflows can also be due to the model resolution. The model resolves a current field within the model domain, which does not perfectly match the actual topography in Førdefjorden. The Førdefjord160 model has 35 vertical levels and terrain-following sigma coordinates in the vertical. The highest vertical resolution is in the surface layer. The bottom depth at the grid points close to the stations is 295 m. The minimum depth between the vertical levels here is 0.6 m and the maximum depth between the vertical levels is 19.3 m. The latter is the difference between 207 m and 226 m depth. The vertical resolution increases in the four lowest levels to 13.6 m depth between the two deepest layers. The terrain-following coordinate system can have errors in the horizontal pressure gradients and the error depends on the steepness of the topography, the strength of the stratification, and the vertical and horizontal resolution (Haidvogel & Beckmann, 1999). Førdefjord160 includes steep topography and it is likely that this error can be present in the model.

Skarðhamar et al. (2018) discuss previous work where Norkyst800 and Norfjords160 have been used to investigate particle drift. The studies conclude that the model resolves general patterns, spatial variability, and mean state compared to observations. The studies concerning salmon lice dispersion reveal that the model system can reproduce the lice infestation levels as observed by the fish farms. Since the STD in Førdefjorden has not started yet, it is not possible to validate the dispersion of particles with observations. However, the model resolves realistic current fields and particle dispersion in various fjord systems in Norway. It is therefore reasonable to assume that the model can be used to investigate the dispersion of mine particles in Førdefjorden.

## 5.2 Dispersion of particles

In my experiments, I released particles at 280 m depth (scenario S1), 250 m depth (S2), 150 m depth (S3), and 100 m depth (S4). Scenarios S1 and S2 had a bathymetry representing the

present bathymetry, while scenarios S3 and S4 included a modified bathymetry representing a bottom after 50 years of tailing disposal. The yearly mean current field comparisons at 100 m and 150 m with the two different bathymetries showed a modest strengthening of the currents in the STD area with shallower bathymetry (Figure 4.9). The calculated annual sedimentation of settled particles implies that the rate of sedimentation inside the disposal area decreases with increasing release depths (Figures 4.12 and 4.13). The calculated annual maximum concentration of pelagic particles shows that there are high concentrations of particles appearing at shallower depths than allowed (Figures 4.14 and 4.15). The daily concentration of pelagic particles shows that the concentration limits set by the regulations (Table 1.1) are frequently met or exceeded in scenarios S3 and S4 (Figures 4.17 and 4.18). Stronger currents in the fjord seem to spread out particles in the whole water column. When the currents weaken, the particles are more confined at certain depths (Figure 4.19).

There are some consistent patterns in the dispersion of particles. The highest concentrations of particles appear on the northern side of the fjord to the west of the STD area (Figures 4.14 and 4.15). Although the figures only show the annual maximum concentration at given depth intervals, they can give an indication of how the particles disperse. The occasions when higher concentrations of particles are present outside the STD site might be connected to events of stronger currents transporting the particles. Due to Earth's rotation, currents flowing out of the fjord will be pushed towards the right in the Northern Hemisphere, which can explain this pattern. Currents are additionally topographically steered. The currents flowing out of the STD area along the bottom on the northern side of the fjord can be affected by the basin west of the STD area, such that they will flow along the basin in a cyclonic motion. Thus, the effects of rotation and topography might explain the settlement of particles in this basin adjacent to the STD site, which is visible in all scenarios (Figures 4.12 and 4.13). To further investigate this, it would be valuable to include the horizontal current field along the bottom of the fjord and at deeper depths than 100 m and 150 m, which were the depths I considered (Figure 4.9).

The results from calculating the annual sedimentation show that the dispersion rate of settled particles increases with decreasing release depth of particles (Figures 4.12 and 4.13). The blue color in the figures displays sedimentation  $\geq 3.0$  mm. The amount of fine fraction of particles is uncertain due to the uncertainty of the flocculation process, which is why I also calculated the sedimentation of 5% fine fraction (Figure 4.13). There is a significant increase in the sedimentation of 5% fine fraction compared to the sedimentation of 1% fine fraction (Figures 4.12 and 4.13). There are fewer particles settling in the STD area when the release depth is shallower for both 1% and 5% fine fractions. This is evident when comparing the scenarios with equal bathymetry. Particles disperse more in scenario S2 than S1, and in scenario S4 compared to S3. The validation of the current field showed that the model underestimates the outflowing current speeds at 150 m depth at all stations across the fjord (Figure 4.8), indicating that particles in reality can potentially disperse further than my results show.

The modified bathymetry used in the future scenarios is based on the assumption of 50 years of mine tailing discharge. It is not certain if this is what the mining company will do, but it is an assumption I have used based on the initial assessment study. The shallowest point of the modified bathymetry is 200 m deep. Nepstad & Rye (2014) releases particles at 155 m depth as their future scenario representing 50 years of STD in Fjørdefjorden. Thus, scenario S3 with a release depth of 150 m depth is probably a realistic scenario, while scenario S4 with a release depth of particles at 100 m is an extreme scenario. Even though S4 is an extreme scenario,

it is interesting to examine how the currents vary in the different depths where particles are released. However, it is hard to distinguish between the effect of changing the bathymetry and changing the release depths in my scenarios. The sedimentation of particles in scenarios S1 and S2 show similar patterns and include the same bathymetry. The release depths are at 280 m and 250 m, which is relatively close and the current fields at these depths might be comparable. The sedimentation in scenarios S3 and S4 are also alike and have equal bathymetry. The difference in release depths is 50 m, and comparing the particle concentration from scenarios S3 and S4 at the same locations reveals differences in the current fields (Figures 4.17 and 4.18). The high concentrations seem to be more confined at shallower depths at all grid points in scenario S4 compared to S3. Moreover, the annual maximum concentrations in scenarios S3 and S4 between 50 m and 60 m depth show substantially more particles in scenario S4 than in scenario S3 (Figures 4.14a and 4.15e). Additionally, at the deepest depths displayed in these figures, which are 40 m above the release depths, the particles seem to drift further away from the STD site in scenario S4. The annual mean current fields at 150 m and 100 m depth also show stronger currents at 100 m depth (Figure 4.9b,d).

There is a distinct larger spread in the settled particles in scenarios S3 and S4 than in scenarios S1 and S2. Since the currents are stronger at 100 m depth than at 150 m depth, there is presumably a considerable difference between the current fields at the two deepest release depths and the two shallowest release depths. It is not evident in the estimated mean values from 282 m and 153 m depth during the current measurement period that there are stronger current velocities higher up in the water column (Table 4.3). However, the estimated mean values are from around the stations, which is west of the STD area. The mean values of the current velocity in the STD area increase slightly with the shallower bathymetry (Figure 4.9c,d). Additionally, the released particles have a constant sinking velocity and there might be higher current velocities at depths between 150 m and 250 m which transports the particles further. Moreover, I did not investigate the effect of a shallower bathymetry on the current field during events of stronger currents. The currents in scenarios S3 and S4 might occasionally be significantly stronger than the currents in scenarios S1 and S2, especially in the STD area. Staalstrøm & Daae (2009) simulated the current field in Fjørdefjorden using ROMS, and examined changes in the current field due to a shallower bathymetry in the STD area during the mean conditions. They find that the current speed can become three times stronger along the bottom at the STD site with shallower bathymetry. Thus, it is possible that it is a combination of a shallower bathymetry and stronger currents higher up in the water column that leads to a larger spread in the settled particles in scenarios S3 and S4 than in scenarios S1 and S2. However, the difference in the mean currents between 100 m depth and 150 m depth is substantially larger than the difference in the mean currents at equal depths but with dissimilar bathymetries (Figure 4.9). Stronger currents at shallower depths might therefore have a larger impact on the particle dispersion than the modified bathymetry.

The concentration of pelagic particles at the selected grid points shows high variability with time (Figures 4.17 and 4.18), which can be caused by various processes. The local wind and freshwater runoff mainly influence the upper 10-20 m of fjords. The tides are a constant forcing that affects all depths and can generate mixing. However, the main driving force of water exchange between the coast and fjords with relatively deep sills is density fluctuations in the coastal water, which can for instance be induced by coastal winds. Asplin et al. (1999) study the importance of coastal wind on the fjord circulation in Masfjorden, which is located south of Fjørdefjorden on the western coast of Norway. They used a coastal ocean model to examine

the effect of coastal upwelling and downwelling on the fjord circulation, which was found to have a direct influence on the water exchange in the fjord. Masfjorden has a sill at 70 m depth, while the sill northeast of Svanøy that connects Førdefjorden to the coastal water is at 210 m depth. It is therefore possible that the coastal wind outside Førdefjorden can generate currents propagating into and out of the fjord at different depths. How frequent these inflows and outflows are, how large the corresponding volume transport is, and how they affect the particle drift in the fjord is uncertain. However, the wind field at the coast and the current field at grid point P4 show higher values in the time before the convergence of particles (Figures 4.19b and 4.20b). The strong wind at the coast might have caused stronger currents in the fjord, which perhaps diluted the concentration of particles in the water masses (Figure 4.19). The concentration of particles is higher and more confined at certain depths after this.

Reartes & Mininni (2023) examine the dispersion and convergence of light inertial particles in stably stratified turbulent flows. The vertical transport of particles is largely confined in layers, which they find to strongly influence the clustering of particles. Additionally, they find that increased stratification enhances the clustering of particles. This can be an explanation of the confinement of particles visible in Figures 4.19(a) and 4.20(a). After the strong winds at the coast and the strong oscillating currents in the fjord that potentially weakened the stratification in the fjord, the currents become weaker and an enhanced stratification is possible. However, I only investigated one event of clustering of particles, and the pattern found is inconclusive. It would be valuable to examine several events of convergence of particles in the water masses and whether there is a common pattern.

I simulated the dispersion of particles with the total weight of  $4 \times 10^7 \text{ kg yr}^{-1}$ , which is uniformly distributed per day during the simulation year. This is probably not how the actual disposal of particles will happen. However, the fine-grained particles will use a few days before they settle on the seafloor in the fjord. Thus, it is important to look at the daily disposal of particles when investigating the particle concentration. If one averages over a larger time span, potentially high concentrations of particles can get filtered out. My results of daily particle concentration show that there are frequently too high concentrations at the grid points outside the STD site (Figures 4.18). If the planned STD discharges more than this annually-averaged amount of particles during a couple of days, it is likely that the concentration of particles can easily exceed the allowed limits.

# Chapter 6

## Conclusions

Through this thesis, I aimed to investigate the dispersion of fine-grained particles in Førdefjorden in terms of three research questions. To achieve this, I used results from the hydrodynamic model Førdefjord160 and the model LADIM to simulate the particle drift in the fjord in four different scenarios. Firstly, I evaluated the model performance of Førdefjord160 compared to observations. Secondly, I calculated the sedimentation of settled particles and the concentration of pelagic particles and analyzed my results in regard to the regulations of the permitted STD.

My first research question was whether the hydrodynamic model can simulate a realistic current field in Førdefjorden comparison with observations. The simulations presented in this thesis suggest this since the range of the modeled current speed and the direction of the modeled currents correspond well with the observed data. Validation of Norkyst800 and Norfjords160 in other regions and fjords also shows that the models simulate realistic current fields. The validation I have done demonstrates that the model represents realistic dynamics in Førdefjorden.

My second research question concerned how changes in bathymetry and release depth of particles affect the particle dispersion in Førdefjorden. I find that the modified bathymetry leads to slightly higher current velocity in the STD site. The change in release depth shows large differences in the dispersion and drift of particles. I find that with decreasing release depth and a shallower bathymetry in the STD site there is an increased rate of dispersion of the particles. This leads to fewer particles settling in the STD site.

The third research question I aimed to investigate was whether the dispersion of fine fraction of particles is pronounced in regards to the regulations. My results from simulating particle dispersion for a year reveal that the fine fraction can lead to higher annual sedimentation outside the STD site than the allowed limits. There are additionally frequently too high daily concentrations of fine-grained particles appearing outside the STD area during the year. Moreover, if the daily amount of discharged tailing as presented here increases, the risk of exceeding the set limits is higher. Thus, this work shows that a fine fraction of 1% of the annual tailing discharge can cause annual sedimentation and daily concentration rates exceeding the given regulations for the permitted STD in Førdefjorden.

## 6.1 Outlook

The two models applied in this work can sufficiently simulate the transport of mine particles in Førdefjorden and can be used to further understand fjord dynamics coupled to particle dispersion both in the present fjord and other fjord systems. The study of the effect of inflow episodes on particle dispersion is for instance limited in this thesis. The deep sill at the mouth of Førdefjorden makes the fjord susceptible to frequent water exchange between the adjacent coastal water and the fjord water. When performing an STD in Førdefjorden, it is therefore crucial to examine the extreme values of the currents in the fjord. How often do inflows of strong currents occur, and at what temporal and spatial scales? The present model can give estimates of this. However, the model is not perfect, and continuous validation is needed for further improvements. More observations of both currents and hydrography in Førdefjorden would be beneficial to perform a more comprehensive validation, which can enhance the understanding of why the model cannot entirely capture the maximum and minimum values of the current speed at depths I investigated.

The model validation performed in this study has the potential for improvements. I calculated the RMSE and the correlation between the simulated and observed current speeds at corresponding hourly values. As previously discussed, the model can be shifted temporally and spatially compared to the observations. Thus, these estimates might not be the best approaches for validating a fjord model. Dalsøren et al. (2020) present a new validation method for comparing fjord model results with observed currents, which would be valuable to implement in future work. Moreover, performing an analysis of the principle components of variance on both the observed and the modeled current speed data could be useful. I only examined two depths, and this type of analysis would indicate at what depths the most variance occurs and whether it coincides between the simulated and observed datasets. This could give additional information about the model performance and a further understanding of the dynamics in Førdefjorden.

The simulation period for both models used in this work lasted for a year. It would be valuable to extend the simulation period to several years to further understand the dynamics in Førdefjorden. Are there evident seasonal patterns in the circulation to consider, such that one should discharge more or fewer particles during these periods? It would also be interesting to study the long-term effects of STD in Førdefjorden, and whether the dispersion patterns are the same after one year and ten years.

It would be interesting to study the effect of the shallower bathymetry and release depths on the particle transport further. A more extensive comparison of the simulated current fields in Førdefjorden from the two different runs would be beneficial to better understand the implications of a shallower bathymetry on the dynamics in the fjord. This can for instance be the influence of a shallower bathymetry on inflow episodes of stronger currents. I investigated four scenarios of particle dispersion, with the main focus on scenarios representing the end of the STD in Førdefjorden. It would be useful to investigate two scenarios with equal release depths but different bathymetries to better distinguish between and determine the effect of shallower release depth and shallower bathymetry on the transport of particles. It could also be interesting to release particles at several release points, for instance to the east of the shallower bathymetry to see if the particles disperse less then.

More research on fjord dynamics in depth and dispersion of mine particles is needed to increase the knowledge of the topic. A better understanding of particle dispersion will enhance the research on the implications of tailings on the marine ecosystem. With increased knowledge of the implications of an STD, a further development of methods for monitoring active STDs is possible, and a more educated decision can be made on whether to conduct new STDs.



# Bibliography

- Aksnes, D. L., Aure, J., Johansen, P. O., Johnsen, G. H., & Salvanes, A. G. V. (2019). Multi-decadal warming of atlantic water and associated decline of dissolved oxygen in a deep fjord. *Estuarine, Coastal and Shelf Science*, 228. <https://doi.org/10.1016/j.ecss.2019.106392>
- Albretsen, J. & Asplin, L. (2021). *RAPPORT FRA HAVFORSKNINGEN NR. 2021-20 HVILKEN BETYDNING HAR OPPLØSNING FOR KYST- OG FJORD-MODELLER? Validering og representasjonsberegninger av strømmodeller med eksempler fra Sulafjorden, Møre og Romsdal.* <https://www.hi.no/hi/nettrapporter/rapport-fra-havforskningen-2021-20>
- Albretsen, J., Sandvik, A. D., Asplin, L., Lien, V., & Skardhamar, J. (2022). *RAPPORT FRA HAVFORSKNINGEN NR. 2022-35 NORKYST800: VERSJONER OG ARKIVER Oversikt over versjoner og arkiver av NorKyst800 som hittil er brukt for modellering av det fysiske miljø i norsk kystsone-med fokus på implikasjoner for lakselusmodellen til Havforskningsinstituttet.* <https://www.hi.no/hi/nettrapporter/rapport-fra-havforskningen-2022-35>
- Albretsen, J., Sperrevik, A. K., Staalstrøm, A., Sandvik, A. D., Vikebø, F., & Asplin, L. (2011). *NorKyst-800 Report No. 1 User Manual and technical descriptions.*
- Anon. (2014). *Rutilutvinning fra Engebøfjellet: Plan for deponering og beskrivelse av avgangssystem.* Nordic Rutile AS.
- Anon. (2023). *Tillatelse til virksomhet etter forurensningsloven for Nordic Rutile AS.* Miljødirektoratet.
- Arneborg, L. (2004). Turnover times for the water above sill level in gullmar fjord. *Continental Shelf Research*, 24, 443–460. <https://doi.org/10.1016/j.csr.2003.12.005>
- Asplin, L., Albretsen, J., Johnsen, I. A., & Sandvik, A. D. (2020). The hydrodynamic foundation for salmon lice dispersion modeling along the norwegian coast. *Ocean Dynamics*, 70, 1151–1167. <https://doi.org/10.1007/s10236-020-01378-0>
- Asplin, L., Gro, A., Salvanes, V., & Kristoffersen, J. B. (1999). Nonlocal wind-driven fjord-coast advection and its potential effect on plankton and fish recruitment. *Fisheries Oceanography*, 8, 255–263.
- Aure, J., Asplin, L., & Sætre, R. (2007). *Coast/fjord water exchange*, 115–124. Tapir Academic Press.
- Aure, J., Ert, M. ., & Stigebrandt, A. (1996). Observations of inshore water exchange forced by a fluctuating offshore density field. *Marine Pollution Bulletin*, 33, 112–119.

- Boyce, W. E. & DiPrima, R. C. (2005). *Elementary Differential Equations and Boundary Value Problems* (8 ed.). John Wiley and Sons, Inc.
- Bruvold, A. S., Bienfait, A. M., Ervik, T. K., Loeschner, K., & Valdersnes, S. (2023). Vertical distribution of inorganic nanoparticles in a norwegian fjord. *Marine Environmental Research*, 188, 105975. <https://doi.org/https://doi.org/10.1016/j.marenvres.2023.105975>
- Cushman-Roisin, B., Asplin, L., & Svendsen, H. (1994). Upwelling in broad fjords. *Continental Shelf Research*, 14(15), 1701–1721.
- Cushman-Roisin, B. & Beckers, J. (2011). *Introduction to Geophysical Fluid Dynamics: Physical and Numerical Aspects* (2 ed.). International Geophysics. Academic Press. <https://books.google.no/books?id=3KS8sD5ky9kC>
- Dagestad, K.-F., Röhrs, J., Breivik, Ø., & Ådlandsvik, B. (2018). Opendrift v1.0: a generic framework for trajectory modelling. *Geoscientific Model Development*, 11(4), 1405–1420. <https://doi.org/10.5194/gmd-11-1405-2018>
- Dalsøren, S. B., Albretsen, J., & Asplin, L. (2020). New validation method for hydrodynamic fjord models applied in the hardangerfjord, norway. *Estuarine, Coastal and Shelf Science*, 246. <https://doi.org/10.1016/j.ecss.2020.107028>
- Dold, B. (2014). Submarine tailings disposal (std)—a review. *Minerals*, 4(3), 642–666. <https://doi.org/10.3390/min4030642>
- Dyer, K. R. (1997). *Estuaries: a physical introduction* (2 ed.). Wiley.
- Egbert, G. D. & Erofeeva, S. Y. (2002). Efficient inverse modeling of barotropic ocean tides. *Journal of Atmospheric and Oceanic Technology*, 19(2), 183 – 204. [https://doi.org/https://doi.org/10.1175/1520-0426\(2002\)019<0183:EIMOB0>2.0.CO;2](https://doi.org/https://doi.org/10.1175/1520-0426(2002)019<0183:EIMOB0>2.0.CO;2)
- Farmer, D. M. & Freeland, H. J. (1983). The physical oceanography of fjords. *Progress in Oceanography*, 12, 147–220.
- Gade, H. G. & Edwards, A. (1980). Deep water renewal in fjords. *Fjord Oceanography*, 453–489. Springer US. [https://doi.org/10.1007/978-1-4613-3105-6\\_43](https://doi.org/10.1007/978-1-4613-3105-6_43)
- Haidvogel, D. B., Arango, H., Budgell, W. P., Cornuelle, B. D., Curchitser, E., Lorenzo, E. D., Fennel, K., Geyer, W. R., Hermann, A. J., Lanerolle, L., Levin, J., McWilliams, J. C., Miller, A. J., Moore, A. M., Powell, T. M., Shchepetkin, A. F., Sherwood, C. R., Signell, R. P., Warner, J. C., & Wilkin, J. (2008). Ocean forecasting in terrain-following coordinates: Formulation and skill assessment of the regional ocean modeling system. *Journal of Computational Physics*, 227, 3595–3624. <https://doi.org/10.1016/j.jcp.2007.06.016>
- Haidvogel, D. B. & Beckmann, A. (1999). *Numerical Ocean Circulation Modeling* (3 ed.). Imperial College Press. <https://doi.org/10.1142/p097>
- Inall, M. E. & Gillibrand, P. A. (2010). The physics of mid-latitude fjords: A review. *Geological Society Special Publication*, 344, 17–33. <https://doi.org/10.1144/SP344.3>
- Johnsen, I. A., Asplin, L. C., Sandvik, A. D., & Llinares, R. M. (2016). Salmon lice dispersion in a northern norwegian fjord system and the impact of vertical movements. *Aquaculture Environment Interactions*, 8, 99–116. <https://doi.org/10.3354/aei00162>

- Kögel, T. (2019). *FØRDEFJORDEN: BASISUNDERSØKELSE AV FREMMEDSTOFF I SJØMAT Analyse av tungmetaller, andre grunnstoff og persistente organiske forbindelser i sjømat fra Førdefjorden 2017.*
- Myksvoll, M. S., Sandvik, A. D., Albretsen, J., Asplin, L., Johnsen, I. A., Ørjan Karlsen, Kristensen, N. M., Melsom, A., Skardhamar, J., & Ådlandsvik, B. (2018). Evaluation of a national operational salmon lice monitoring system—from physics to fish. *PLoS ONE*, 13. <https://doi.org/10.1371/journal.pone.0201338>
- Myksvoll, M. S., Sundby, S., Ådlandsvik, B., & Vikebø, F. B. (2011). Retention of coastal cod eggs in a fjord caused by interactions between egg buoyancy and circulation pattern. *Marine and Coastal Fisheries*, 3, 279–294. <https://doi.org/10.1080/19425120.2011.595258>
- Müller, M., Homleid, M., Ivarsson, K. I., Køltzow, M. A., Lindskog, M., Midtbø, K. H., Andrae, U., Aspelien, T., Berggren, L., Bjørge, D., Dahlgren, P., Kristiansen, J., Randriamampianina, R., Ridal, M., & Vignes, O. (2017). Arome-metcoop: A nordic convective-scale operational weather prediction model. *Weather and Forecasting*, 32, 609–627. <https://doi.org/10.1175/WAF-D-16-0099.1>
- Nepstad, R. & Rye, H. (2014). *Simuleringer av partikkelspredning i Førdefjorden fra planlagt sjødeponi.*
- Nortek (2018). *Signature Principles of Operation.* <https://www.nortekgroup.com/>
- Omholt, M., Finn, A., Michelsen, A., & Ellingsen, I. H. (2014). *Strømmodellering med SINMOD i Førdefjorden.*
- Ramirez-Llodra, E., Trannum, H. C., Andersen, G. S., Baeten, N. J., Brooks, S. J., Escudero-Oñate, C., Gundersen, H., Kleiv, R. A., Ibragimova, O., Lepland, A., Nepstad, R., Sandøy, R., Schaanning, M. T., Shimmield, T., Yakushev, E., Ferrando-Climent, L., & Høgaas, P. H. (2022). New insights into submarine tailing disposal for a reduced environmental footprint: Lessons learnt from norwegian fjords. *Marine Pollution Bulletin*, 174, 113150. <https://doi.org/https://doi.org/10.1016/j.marpolbul.2021.113150>
- Ramirez-Llodra, E., Trannum, H. C., Evenset, A., Levin, L. A., Andersson, M., Finne, T. E., Hilario, A., Flem, B., Christensen, G., Schaanning, M., & Vanreusel, A. (2015). Submarine and deep-sea mine tailing placements: A review of current practices, environmental issues, natural analogs and knowledge gaps in norway and internationally. *Marine Pollution Bulletin*, 97(1), 13–35. <https://doi.org/https://doi.org/10.1016/j.marpolbul.2015.05.062>
- Reartes, C. & Mininni, P. D. (2023). Dynamical regimes and clustering of small neutrally buoyant inertial particles in stably stratified turbulence. *PHYSICAL REVIEW FLUIDS*, 8(5). <https://doi.org/10.1103/PhysRevFluids.8.054501>
- Rygg, B. (2007). *Dyrelivet på bunnen av Førdefjorden og bunnsedimentenes sammensetning.* [www.niva.no](http://www.niva.no)
- Sandvik, A. D., Bjørn, P. A., Ådlandsvik, B., Asplin, L., Skardhamar, J., Johnsen, I. A., Myksvoll, M., & Skogen, M. D. (2016). Toward a model-based prediction system for salmon lice infestation pressure. *Aquaculture Environment Interactions*, 8, 527–542. <https://doi.org/10.3354/AEI00193>

- Shchepetkin, A. F. & McWilliams, J. C. (2005). The regional oceanic modeling system (roms): a split-explicit, free-surface, topography-following-coordinate oceanic model. *Ocean Modelling*, 9(4), 347–404. <https://doi.org/https://doi.org/10.1016/j.ocemod.2004.08.002>
- Shchepetkin, A. F. & McWilliams, J. C. (2009). Computational kernel algorithms for fine-scale, multiprocess, longtime oceanic simulations. *Special Volume: Computational Methods for the Atmosphere and the Oceans*, volume 14 of *Handbook of Numerical Analysis*, 121–183. Elsevier. [https://doi.org/https://doi.org/10.1016/S1570-8659\(08\)01202-0](https://doi.org/https://doi.org/10.1016/S1570-8659(08)01202-0)
- Skarðhamar, J., Albretsen, J., Sandvik, A. D., Lien, V. S., Myksvoll, M. S., Johnsen, I. A., Asplin, L., Ådlandsvik, B., Halttunen, E., & Bjørn, P. A. (2018). Modelled salmon lice dispersion and infestation patterns in a sub-arctic fjord. *ICES Journal of Marine Science*, 75, 1733–1747. <https://doi.org/10.1093/icesjms/fsy035>
- Skogen, M. D., Ji, R., Akimova, A., Daewel, U., Hansen, C., Hjøllø, S. S., Leeuwen, S. M. V., Maar, M., Macias, D., Mousing, E. A., Almroth-Rosell, E., Sailley, S. F., Spence, M. A., Troost, T. A., & de Wolfshaar, K. V. (2021). Disclosing the truth: Are models better than observations? *Marine Ecology Progress Series*, 680, 7–13. <https://doi.org/10.3354/meps13574>
- Staalstrøm, A. & Daae, K. (2009). *Strømforhold i Førdefjorden utenfor Engebøfjellet: Tredimensjonal modellering av strømforholdene i vannsøylen ved endring av bunntopograf*. [www.niva.no](http://www.niva.no)
- Staalstrøm, A. & Molvær, J. (2009). *Spredning av partikler i overflatelaget utenfor Engebøfjellet*. [www.niva.no](http://www.niva.no)
- Stigebrandt, A. (2012). Hydrodynamics and circulation of fjords. *Encyclopedia of Lakes and Reservoirs*, 327–344. Springer Netherlands. [https://doi.org/10.1007/978-1-4020-4410-6\\_247](https://doi.org/10.1007/978-1-4020-4410-6_247)
- Sætre, R. (2007a). *The Norwegian Coastal Current: Oceanography and Climate*. Tapir Academic Press.
- Sætre, R. (2007b). *Short-term variability and small-scale features*, 89–98. Tapir Academic Press.
- Thomson, R. E. & Emery, W. J. (2014). Chapter 3 - statistical methods and error handling. *Data Analysis Methods in Physical Oceanography (Third Edition)*, 219–311. Elsevier, (third edition ed.). <https://doi.org/https://doi.org/10.1016/B978-0-12-387782-6.00003-X>
- Tinis, S. W. & Pond, S. (2001). Tidal energy dissipation at the sill of sechelt inlet, british columbia. *Journal of physical oceanography*, 31.
- Vare, L. L., Baker, M. C., Howe, J. A., Levin, L. A., Neira, C., Ramirez-Llodra, E. Z., Reichelt-Brushett, A., Rowden, A. A., Shimmield, T. M., Simpson, S. L., & Soto, E. H. (2018). Scientific considerations for the assessment and management of mine tailings disposal in the deep sea. *FRONTIERS IN MARINE SCIENCE*, 5. <https://doi.org/10.3389/fmars.2018.00017>

- Vogelsang, C. & Bjerkeng, B. (2014). *Utsynkingsforsøk med flokkulert avgang fra Engebøfjellet*. [www.niva.no](http://www.niva.no)
- Ådlandsvik, B. (2022). *LADiM Documentation Release 1.1.0*. [https://ladim.readthedocs.io/\\_/downloads/en/master/pdf/](https://ladim.readthedocs.io/_/downloads/en/master/pdf/)
- Ådlandsvik, B. (2023). *ROPpy - ROMS post-processing tools in python*. <https://github.com/bjornaa/roppy>. Accessed: 09.10.2023.
- Ådlandsvik, B. & Sundby, S. (1994). Modeling the transport of cod larvae from the lofoten area. *ICES Marine Science Symposia*, 198, 379–392.



# **Appendix A**

## **Moorings**

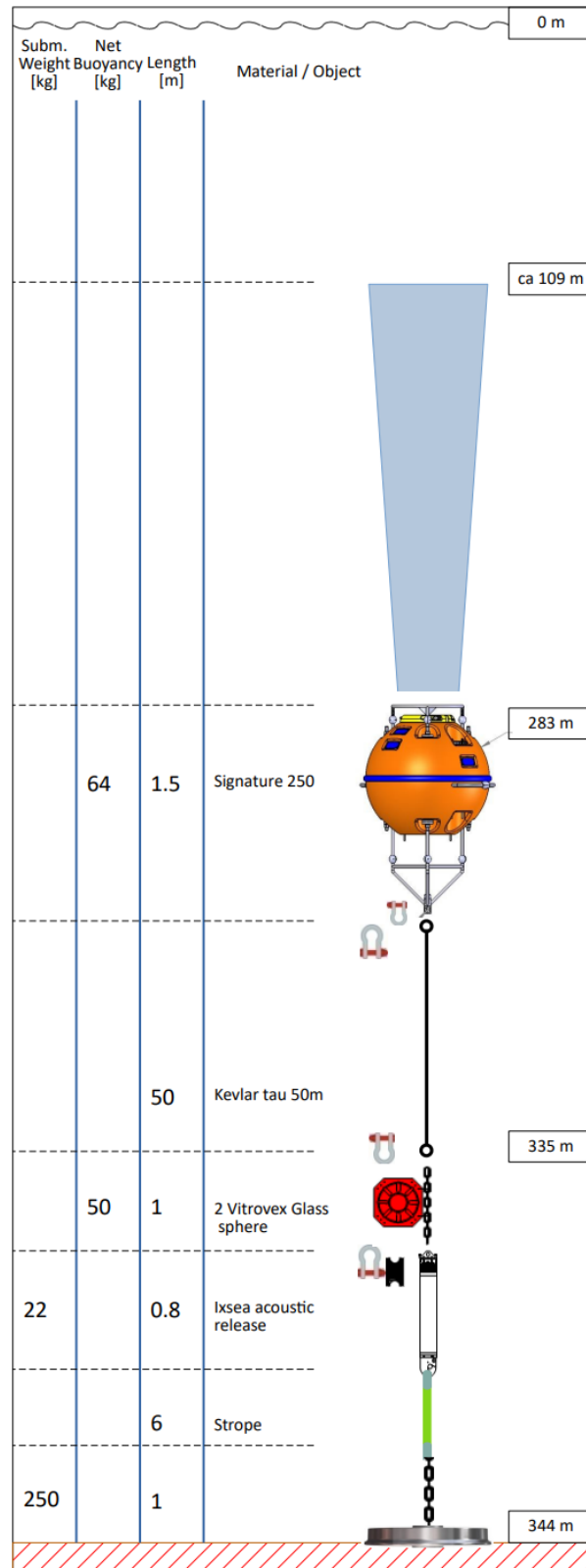


Figure A.1: Schematic of the moored instruments at the middle position in Fjørdefjorden. Source: IMR.

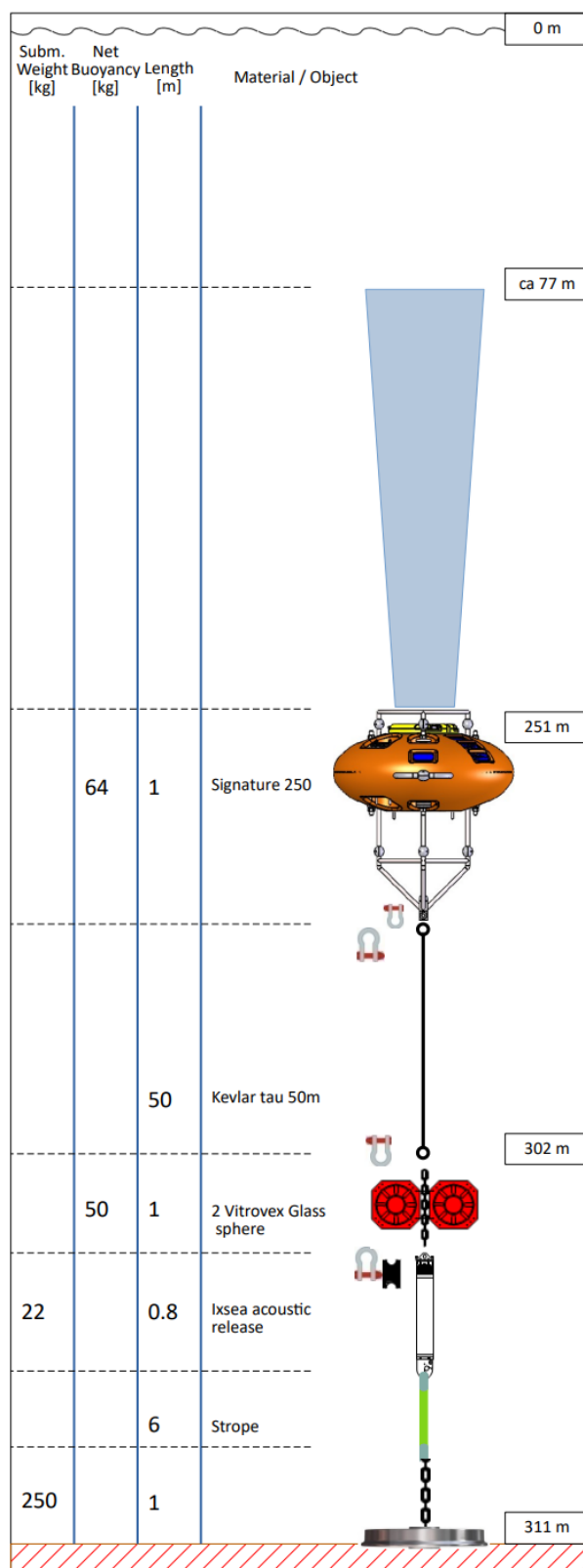


Figure A.2: Schematic of the moored instruments at the southern position in Fjørdefjorden.  
Source: IMR.



# Appendix B

## CTD stations

*Table B.1: Location, date and depth of the ctd-profiles. The letter in the station names implies which month the station is taken in.*

| St. | Lat [°N] | Lon [°E] | Date     | Profile depth [m] |
|-----|----------|----------|----------|-------------------|
| O1  | 61.484   | 5.328    | 10.03.21 | 303               |
| D1  | 61.488   | 5.299    | 13.12.21 | 334               |
| F1  | 61.487   | 5.354    | 16.02.22 | 344               |



# Appendix C

## Annual current field at the stations

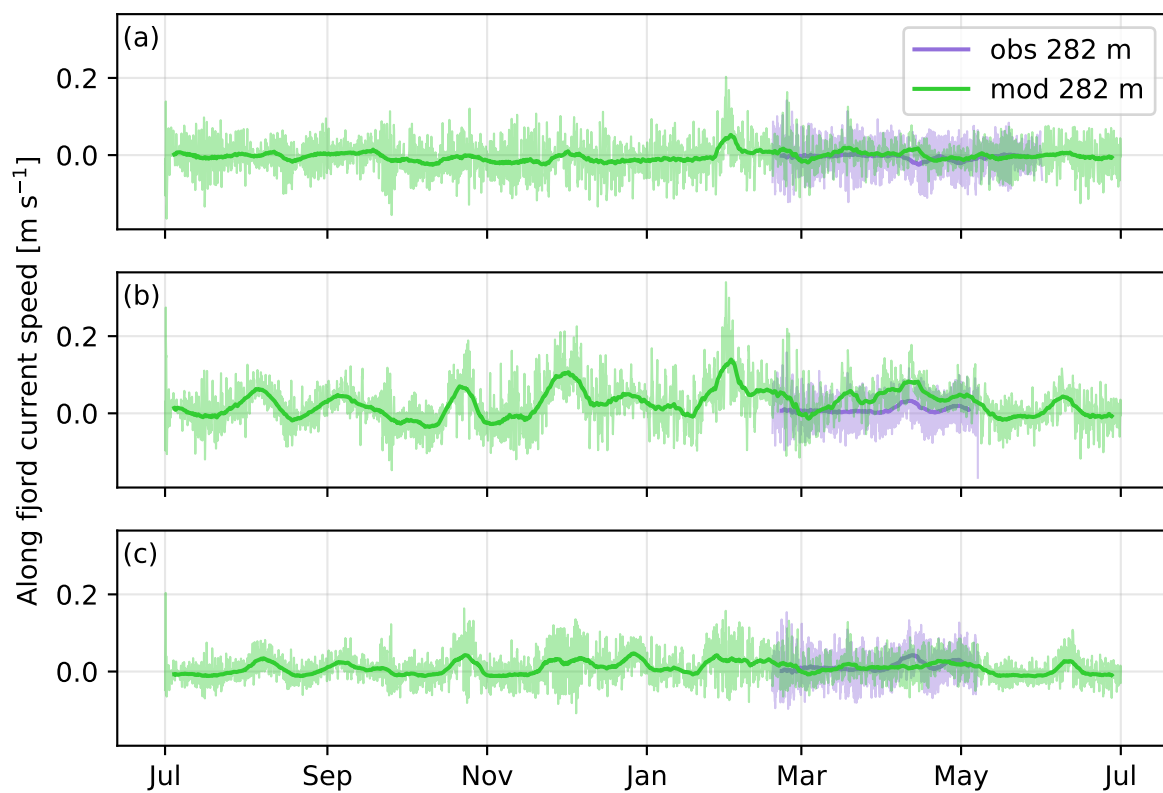


Figure C.1: Simulated along fjord current speed from the whole simulation period and the observed along fjord current speed from February to May 2022 at station N (a), station M (b), and station S (c) at 282 m depth. The bold lines represent filtered data with a weekly running mean filter, and the thin lines present the raw data. Current speed  $> 0.0\text{m s}^{-1}$  is directed into the fjord and current speed  $< 0.0\text{m s}^{-1}$  is directed out of the fjord.